Extension and Comparative Study of AUSM-Family Schemes for Compressible Multiphase Flow Simulations

Keiichi Kitamura[1,2,*], Meng-Sing Liou[1] and Chih-Hao Chang[3]

[1] *NASA Glenn Research Center, Cleveland, OH 44135, USA.*
[2] *Research Fellow of Japan Society for the Promotion of Science (JSPS), JAXA's Engineering Digital Innovation (JEDI) Center, 3-1-1 Yoshinodai, Chuo, Sagamihara, Japan; Previously at Nagoya University, Furo-cho, Chikusa-ku, Nagoya, Aichi 464-8603 Japan; Currently at Yokohama National University, 79-5 Tokiwadai, Hodogaya-ku, Yokohama 240-8501, Japan.*
[3] *Theofanous & Co Inc. Santa Barbara, CA 93109, USA.*

Abstract. Several recently developed AUSM-family numerical flux functions (SLAU, SLAU2, AUSM$^+$-up2, and AUSMPW+) have been successfully extended to compute compressible multiphase flows, based on the stratified flow model concept, by following two previous works: one by M.-S. Liou, C.-H. Chang, L. Nguyen, and T.G. Theofanous [AIAA J. 46:2345-2356, 2008], in which AUSM$^+$-up was used entirely, and the other by C.-H. Chang, and M.-S. Liou [J. Comput. Phys. 225:840-873, 2007], in which the exact Riemann solver was combined into AUSM$^+$-up at the phase interface. Through an extensive survey by comparing flux functions, the following are found: (1) AUSM$^+$-up with dissipation parameters of K_p and K_u equal to 0.5 or greater, AUSMPW+, SLAU2, AUSM$^+$-up2, and SLAU can be used to solve benchmark problems, including a shock/water-droplet interaction; (2) SLAU shows oscillatory behaviors [though not as catastrophic as those of AUSM$^+$ (a special case of AUSM$^+$-up with $K_p=K_u=0$)] due to insufficient dissipation arising from its ideal-gas-based dissipation term; and (3) when combined with the exact Riemann solver, AUSM$^+$-up ($K_p=K_u=1$), SLAU2, and AUSMPW+ are applicable to more challenging problems with high pressure ratios.

AMS subject classifications: 76T10, 76M12, 76N99

Key words: Multiphase flow, two-fluid model, AUSM-family, stratified flow model.

*Corresponding author. *Email addresses:* `kitamura@ynu.ac.jp` (K. Kitamura), `meng-sing.liou@nasa.gov` (M.-S. Liou), `chchang@theofanous.net` (C.-H. Chang)

Nomenclature

a	=	speed of sound [m/s]
α	=	volume fraction
C_p	=	specific heat at constant pressure, 1004.5 for air and 4186 for water [J/(kg K)]
C_p^*	=	interfacial pressure coefficient, 2.0
χ	=	function in SLAU
E	=	total energy per unit mass [J/kg]
$\mathbf{E,F}$	=	inviscid (numerical) flux vectors in x and y directions, respectively
ε	=	small positive value, such as 10^{-7}
g	=	gravity constant, 9.8 [m/s^2], or function in SLAU
G	=	cubic function
γ	=	specific heat ratio, 1.4 for air and 2.8 for water
H	=	total enthalpy [J/kg]
K_p, K_u	=	dissipation coefficients in AUSM$^+$-up
M	=	Mach number
p	=	pressure [Pa]
PR	=	pressure ratio, p_L/p_R
$\mathbf{Q}$	=	conservative variable vector
ρ	=	density [kg/m^3]
S	=	area of cell interface [m^2]
T	=	temperature [K]
V	=	cell volume [m^3], or velocity [m/s]
u,v	=	velocity components in Cartesian coordinates [m/s]
x,y	=	Cartesian coordinates [m]

Subscripts

L, R	=	left and right running wave components
g	=	gas phase
j	=	(current) cell index
k	=	k-th phase ($k=1, 2$ or g,l)
l	=	liquid phase
n	=	normal component to cell interface
m	=	Newton iteration stage
∞	=	freestream or reference value
1/2	=	cell-interfacial value

Superscripts

int	=	interfacial value
max, min	=	maximum and minimum values
$+, -$	=	left- and right-side values at cell interface
$^-$	=	arithmetically averaged value of both sides at cell interface

1   Introduction

Although the present computational fluid dynamics (CFD) technologies for compressible flows enable us to simulate a wide variety of flow physics, we still have issues in dealing with high- and low-speed flows:

  1) High-speed flows ($M > 1.5$, super- and hypersonic): Shock anomalies [1–4], diffi-
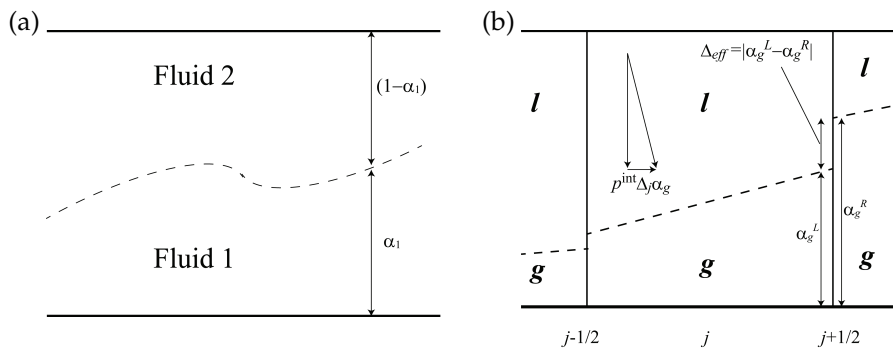
Figure 1: Illustrations of stratified flow model concept (g: gas, l: liquid), (a) Generic; (b) 1D, discretized.

culty in wall-heating prediction [5–8].

2) Low-speed flows ($M < 0.1$, nearly incompressible): convergence difficulty [9, 10] and dissipation control [11, 12] (still debated, specifically in unsteady cases [13]).

In addition, these flow regimes sometimes coexist in realistic problems and/or multiphase flows — this is why it is desirable to pursue a universally usable method for high-speed, low-speed, and multiphase flows, and we feel AUSM-family schemes are promising because they possess the following features:

1) They are robust and accurate for resolving shock waves at *high speeds* [4,7,8].

2) All speed variants (e.g., AUSM$^+$-up, SLAU2) are available that are applicable to *low speeds* [11,12,14,15].

3) No differentiation of a flux function or its eigenstructure is required, hence allowing a straightforward application to complex equation-of-state (EOS) of *multiphase flows* [16].

In the past decade, several attempts have been made to extend AUSM-family schemes to multiphase flow computations with success (e.g., in [16–20]). Among them, the following two novel approaches should be noted, both falling into two-fluid modeling (also known as effective-fluid modeling, EFM), based on the stratified flow model concept (Fig. 1) [17, 21]. It is noted that these two concepts are referred respectively to as Group 1 and Group 2 frequently throughout the paper.

1) Group 1 — AUSM-family standalone: In [16] AUSM$^+$-up [11] flux function, one of the AUSM-family schemes [11,12,15,22–24], was successfully extended from the single-phase version without relying upon an expensive, exact Riemann solver [25]. By allowing difference of volume fractions α at a cell interface, we only need the flux of the same phase (i.e., gas-gas or liquid-liquid) (Figs. 2a, b).

2) Group 2 — AUSM-family coupling with exact Riemann (Godunov) solver: In [17] AUSM$^+$-up was used only to account for the subcell interface of same phases, and
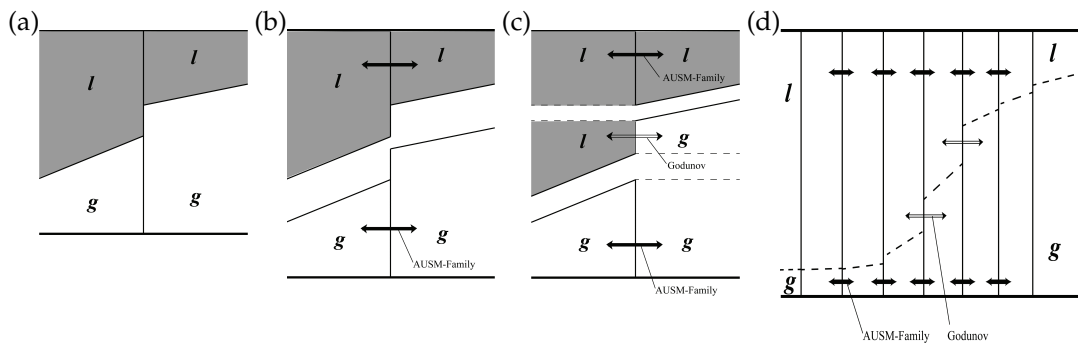
Figure 2: (a) Cell interface in stratified flow concept, (b) Schematic of a standalone AUSM-family scheme (Group 1, or Group 2 in case of small void fraction jump) [16], (c) Schematic of AUSM-family scheme combined with Godunov (Group 2 in case of large void fraction jump) [17], (d) Schematic of Group 2.

the Godunov solver was used for the portion of different phases. This approach utilizes iterations, as is well known, and can accurately predict which of the phases will penetrate into the other at the next time step (i.e., whether the gas flows into the liquid region, or the reverse, at the gas-liquid interface) (Figs. 2a-d).

A natural question to ask is how these two solution strategies differ in solution accuracy, robustness, and so forth. In addition, AUSM-family fluxes, including recently-added SLAU [12], AUSMPW+ [24], have been extensively studied and are known to give robust and accurate solutions efficiently in single-phase gas flows from low speed to hypersonic, but *for multiphase flows extensions and comparisons of the AUSM-family schemes have yet to be conducted.*

Let us briefly review some recent representative multiphase-flow computations for a wide range of applications [26–41], such as for cavitation over underwater airfoils and propellers, rocket engine turbopumps (aerospace or naval engineering), kidney stone removal by shock (medical), detonation (mechanical), and cooling system in the nuclear reactor at high pressure (nuclear). Two approaches can be delineated in terms of treating phase interfaces: first, the interface-sharpening method (level set, front tracking, or volume of fluid) and second, the interface-capturing methods (one-fluid or two-fluid modeling) (see Fig. 3). The former method employs an additional step to recognize the location of interface and imposes a numerically smoothed representation of jumps across the interface. Thus, it is accurate in dealing with, for instance, a single bubble, but will be too expensive when applied to multiple bubbles. What is more, it cannot track creation or collapse of such phase interfaces. The latter method however, captures interface discontinuities as part of numerical solution, but the jumps are smeared over a number of mesh points, largely depending on the numerical flux functions and order of accuracy in discretization. Because of not using "tracking" devices, the interface-capturing approach is "the most practical approach" for dealing with complex geometries like turbopumps, as stated in [42], and also it is able to deal with dynamic creation of cavitation [38]. As
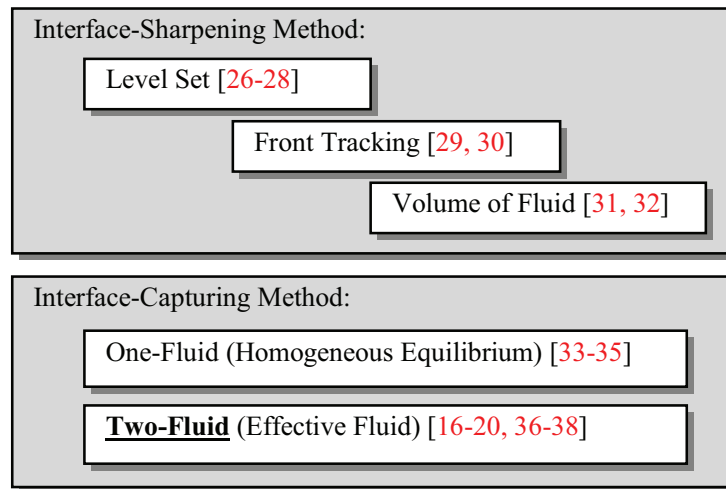
Figure 3: Various methods for multiphase flow computations.

the one-fluid modeling is shown to be inadequate for accurate reproduction of cavitation dynamics, we chose to use the so-called two-fluid modeling, which allows each fluid to possess its own physical variables except for pressure, whereas its one-fluid counterpart deals with averaged (mixture) density and other common variables, causing difficulties in its own justification under some circumstances [36].

Thus, in pursuit of a better option of numerical methods, *we will extend the recently developed flux functions of AUSM-family* [11, 12, 15, 22–24] *to solve multiphase flows in both Groups 1 and 2 via two-fluid modeling*. We will compare their performances in various benchmark tests, and *demonstrate how one method is superior to another* (including comparisons of Group 1 and Group 2). The results and discoveries herein will provide users with guidelines on choosing methods, and also give algorithm researchers direction and motivation for further developments of numerical modeling towards more realistic flow simulations.

2 Numerical methods

2.1 Two-Fluid Modeling (or Effective-Fluid Modeling, EFM)

The 2D compressible Euler equations in two-fluid modeling (or effective-fluid modeling, EFM) are written as:

$$\frac{\partial \mathbf{Q}_k}{\partial t} + \frac{\partial \mathbf{E}_k}{\partial x} + \frac{\partial \mathbf{F}_k}{\partial y} = \mathbf{P}_k^{\text{int}} + \mathbf{S}_k, \quad k = 1, 2, \tag{2.1a}$$

$$\mathbf{Q}_k = \begin{bmatrix} \alpha\rho \\ \alpha\rho u \\ \alpha\rho v \\ \alpha\rho E \end{bmatrix}_k, \quad \mathbf{E}_k = \begin{bmatrix} \alpha\rho u \\ \alpha\rho u^2 + \alpha p \\ \alpha\rho uv \\ \alpha\rho uH \end{bmatrix}_k, \quad \mathbf{F}_k = \begin{bmatrix} \alpha\rho v \\ \alpha\rho vu \\ \alpha\rho v^2 + \alpha p \\ \alpha\rho vH \end{bmatrix}_k,$$

$$\mathbf{P}_k^{\text{int}} = \begin{bmatrix} 0 \\ p^{\text{int}}\frac{\partial\alpha}{\partial x} \\ p^{\text{int}}\frac{\partial\alpha}{\partial y} \\ -p^{\text{int}}\frac{\partial\alpha}{\partial t} \end{bmatrix}_k, \quad \mathbf{S}_k = \begin{bmatrix} 0 \\ \alpha\rho g_x \\ \alpha\rho g_y \\ \alpha\rho g_x u + \alpha\rho g_y v \end{bmatrix}_k, \tag{2.1b}$$

and

$$\alpha_g + \alpha_l = 1, \tag{2.2}$$

$$p_g = p_l \equiv p, \tag{2.3}$$

$$p_g^{\text{int}} = p_l^{\text{int}} \equiv p^{\text{int}}, \tag{2.4}$$

$$p^{\text{int}} = p - \delta p^*, \tag{2.5}$$

where α is the volume fraction of a fluid, ρ the density, u and v are the velocity components in Cartesian coordinates, E is the total energy per unit mass $[E = e + (p/\rho)$, e being the internal energy], p is the pressure, H is the total enthalpy $[H = E + (p/\rho)]$, and g_x and g_y are the x- and y-components of the gravity vector (of magnitude 9.8 m/s^2). Since we treat only gas-liquid systems in this study, $k = 1,2$ is interchangeable with $k = g,l$, where g represents gas and l represents liquid. As in single-fluid equations, $\mathbf{Q}$ is the conservative-variable vector; $\mathbf{E}$ and $\mathbf{F}$ are the inviscid flux vectors in the x- and y-directions, respectively, but with α included; p_k^{int} is the so-called interface pressure, and $\mathbf{S}_k$ is the source term containing the gravity force considered in the "Faucet" problem in this study. The Eq. (2.2) expresses the compatibility relation for volume fractions, Eq. (2.3) and Eq. (2.4) assume pressure equilibrium, and Eq. (2.5) gives interface pressure, p^{int}, as a departure from p by δp^*, which will be explained further in Section 2.3. Now we have 14 unknowns $[\alpha, \rho, u, v, e, p, p^{\text{int}}]_k$ closed by 12 equations [Eqs. (2.1)-(2.5)] with two EOSs described later in Section 2.4.

2.2   Stratified flow model and discretization

Within the framework of a finite-volume, shock-capturing method, we follow the concept of stratified flow model, which was proposed first by Stewart and Wendroff [21] (Fig. 1a) and later refined by Chang and Liou [17] and Liou et al. [16], for constructing a discrete model consistent with the continuous equations, Eq. (2.1). Hence, it is clear to interpret that the interfacial pressure p^{int} must work only within each computation cell, and the volume fractions are assumed to be continuous within the cell but are allowed a jump

at the cell boundaries (Fig. 1b). The discretized form of Eq. (1), by retaining only the 1D form for illustration, is expressed as:

$$\frac{V_j}{\Delta t}\Delta \mathbf{Q}_j + \mathbf{E}_{j+1/2}S_{j+1/2} - \mathbf{E}_{j-1/2}S_{j-1/2} = p_j^{\text{int}} \begin{bmatrix} 0 \\ \alpha_{j+1/2,L} - \alpha_{j-1/2,R} \\ \frac{V_j\left(\alpha_j^{n+1} - \alpha_j^n\right)}{\Delta t} \end{bmatrix} + \mathbf{S}_j, \qquad (2.6)$$

where the phase-subscript k is omitted, and j is the cell index, V_j is the volume of cell j, and $S_{j+1/2}$ is the area of the interface between cells j and $j+1$. All cell-interface variables (such as $\alpha_{j+1/2,L}$) are calculated by the spatially second-order accurate MUSCL interpolation [43] with Van Albada's limiter [44] (limiter coefficient is set as 10^{-20}; limiter effects will be surveyed later in Section 3.1). Note that the present method is valid only for the second-order or higher accuracy, because the first-order reconstruction yields $\alpha_{j+1/2,L} = \alpha_{j-1/2,R} = \alpha_j$ (i.e., no interface pressure acting within a cell). A three-stage, third-order total-variation-diminishing (TVD) Runge-Kutta method [45] is used for time integration, and its details will be explained later in Section 2.6. The numerical code is extended from a single-fluid version previously used by Kitamura et al. [4].

2.3   Interface pressure

The interface pressure, p^{int}, introduced by Stuhmiller [46], working at a phase interface *within* a cell according to Liou et al. (Fig. 1b) [16], is expressed as:

$$p^{\text{int}} = p - \delta p^*,$$

and for a gas-liquid system, δp^* is usually given by

$$\delta p^* = \delta \frac{\alpha_g \alpha_l \rho_g \rho_l}{\alpha_g \rho_l + \alpha_l \rho_g} \left| \mathbf{u}_l - \mathbf{u}_g \right|^2, \qquad (2.7)$$

or after assuming $\rho_l \gg \rho_g$ and (α_l, α_g) are finite, it is simply

$$\delta p^* = C_p^* \alpha_l \rho_g \left| \mathbf{u}_l - \mathbf{u}_g \right|^2. \qquad (2.8)$$

The interface pressure coefficient, C_p^* or δ , should be large enough (at least larger than or equal to unity) to keep the system hyperbolic [16, 39]. We will make use of the simplified form Eq. (2.8) with $C_p^* = 2.0$ (a discussion about the effect of this and other values is given in [16]).

Furthermore, in order to prevent p^{int} from deviating too much from the static pressure p, a limit should be imposed so that δp^* does not exceed a fraction of p:

$$\delta p^* = \min\left(\delta p^*, \varepsilon_p p\right), \qquad (2.9)$$

where the value of $\varepsilon_p = 0.01$ suggested in [17] is also adopted for all the numerical tests here.

2.4   Equation of State (EOS)

For closure of the system we adopted the stiffened-gas model proposed by Harlow and Amsden [47] to represent the EOS:

$$p_k = \rho_k \frac{\gamma_k - 1}{\gamma_k} C_{pk} T_k - p_{k\infty}, \tag{2.10a}$$

$$e_k = \frac{C_{pk}}{\gamma_k} T_k + \frac{p_{k\infty}}{\rho_k}, \tag{2.10b}$$

$$a_k = \left(\frac{\gamma_k (p_k + p_{k\infty})}{\rho_k} \right)^{1/2}, \tag{2.10c}$$

where e_k is the internal energy per unit mass of fluid k and a_k is the speed of sound. It is noted that the standard ideal gas becomes a subset of the stiffened gas, hence it is used to describe both gas and liquid states only with different parameter values [16]:

$$\gamma_g = 1.4, \quad C_{pg} = 1004.5 \text{ [J/(kg K)]}, \quad p_{g\infty} = 0 \text{ [Pa]} \qquad \text{for gas,} \tag{2.11a}$$

$$\gamma_l = 2.8, \quad C_{pl} = 4186 \text{ [J/(kg K)]}, \quad p_{l\infty} = 8.5 \times 10^8 \text{ [Pa]} \quad \text{for liquid.} \tag{2.11b}$$

It is reported by Jolgam et al. in [48] that although the stiffened-gas EOS is relatively simple, it has almost the same accuracy as more sophisticated EOSs (e.g., Tait's EOS for water and van der Waals's EOS for air) in several benchmark tests.

2.5   Numerical fluxes

AUSM-family flux functions of AUSM[+]-up [11], SLAU [12], SLAU2 [15], AUSM[+]-up2 [23], or AUSMPW+ [24] are used to calculate inviscid numerical fluxes at cell interfaces for each phase, denoted as $\mathbf{F}_{k,1/2,L/R}$, where L and R indicate left and right cells, respectively. The numerical flux (except for AUSMPW+) is commonly expressed as:

$$\mathbf{F}_{k,1/2,L/R} = \frac{\dot{m}_{k,1/2} + |\dot{m}_{k,1/2}|}{2} \mathbf{\Psi}_{k,L} + \frac{\dot{m}_{k,1/2} - |\dot{m}_{k,1/2}|}{2} \mathbf{\Psi}_{k,R} + \alpha_{k,1/2,L/R} \tilde{p}_{k,1/2} \mathbf{N}, \tag{2.12a}$$

$$\mathbf{\Psi}_k = (\alpha, \alpha u, \alpha v, \alpha H)_k^T, \quad \mathbf{N} = (0, n_x, n_y, 0)^T. \tag{2.12b}$$

It is noted again that different void fractions exist to the left and right of an interface, and the last term in Eq. (2.12a) will contribute differently; that is, different numerical fluxes $\mathbf{F}_{k,1/2,L}$ and $\mathbf{F}_{k,1/2,R}$, to the left and right cells, respectively. In the case of single-phase flux, it becomes common to both sides and is a special case of the above formula, because void fraction is constant.

As stated in Introduction, only AUSM-family fluxes are used in its entirety in Group 1 [16], whereas the exact Riemann (Godunov) solver is also combined in Group 2 [17]. In Group 2, the Godunov solver is used only when the difference of volume fraction at a cell interface (or "effective length," $\Delta_{eff} = |\alpha_{g,1/2,L} - \alpha_{g,1/2,R}|$) is above a threshold, say, ε:

- if $\Delta_{eff} = |\alpha_{g,1/2,L} - \alpha_{g,1/2,R}| < \varepsilon$: an AUSM-family flux is used everywhere;
- *otherwise*: AUSM-family is used for gas-gas and liquid-liquid interfaces, and Godunov is used elsewhere.

One slight difference of the present Group 2 from [17] is that the former uses AUSM-family fluxes even at a small jump of the volume fraction, whereas the latter used a simple upwind scheme when $0 < |\alpha_{g,1/2,L} - \alpha_{g,1/2,R}| < \varepsilon$.

These two Groups are illustrated in Fig. 2: In either case, at least one AUSM-family flux is used. These schemes [12–15, 23, 24] have showed satisfactory performance in single-phase gas flows from low speed to hypersonic but have not been fully surveyed in multiphase flows yet. Thus, we include in the following the multiphase-flow versions of those fluxes.

2.5.1 AUSM$^+$-up

First, AUSM$^+$-up by Liou [11] for multiphase flows [16] is briefly reviewed as follows. The mass flux is given by

$$(\dot{m}_{k,1/2})_{AUSM^+-up} = M_{k,1/2} a_{1/2} \begin{cases} \rho_{k,L} & \text{if } M_{k,1/2} > 0, \\ \rho_{k,R} & \text{otherwise}, \end{cases} \tag{2.13a}$$

$$M_{k,1/2} = \mathrm{M}_{(4)k}^+ (M_{k,L}) \Big|_{\beta=1/8} + \mathrm{M}_{(4)k}^- (M_{k,R}) \Big|_{\beta=1/8} + M_{pk}, \tag{2.13b}$$

$$\mathrm{M}_{(4)}^\pm (M) \Big|_\beta = \begin{cases} \frac{1}{2}(M \pm |M|), & \text{if } |M| \geq 1, \\ \pm\frac{1}{4}(M \pm 1)^2 \pm \beta (M^2 - 1)^2, & \text{otherwise}, \end{cases} \tag{2.13c}$$

$$M_{pk} = -\frac{K_p}{f_a} \max\left(1 - \bar{M}_k^2, 0\right) \frac{p_R - p_L}{\bar{\rho}_k a_{1/2}^2}, \quad \bar{\rho}_k = \frac{\rho_{k,L} + \rho_{k,R}}{2}, \tag{2.13d}$$

$$M_k = \frac{V_{k,n}}{a_{1/2}} = \frac{u_k n_x + v_k n_y}{a_{1/2}}, \tag{2.13e}$$

$$\bar{M}_k^2 = \frac{V_{k,n}^{+2} + V_{k,n}^{-2}}{2a_{1/2}^2}, \tag{2.13f}$$

where $f_a = 1$ here (hence, no prescribed Mach number is used), and the speed of sound, $a_{1/2}$, common to gas and liquid [16], is

$$a_{1/2} = \frac{1}{2}\left(a_{l,1/2} + a_{g,1/2}\right), \tag{2.13g}$$

$$a_{k,1/2} = \bar{a}_k = \frac{a_{k,L} + a_{k,R}}{2}, \tag{2.13h}$$

where the arithmetic mean of the left and right states is used for the speed of sound for each fluid, $a_{k,1/2}$. We recognize that other forms for providing the interface speed of sound $a_{k,1/2}$ (e.g., a geometric mean of left and right states) are possible; the effect of using different forms of $a_{1/2}$ is beyond the focus of the present paper and hence not

discussed here. Nevertheless, we confirmed in this study that the present choice gives robust performances to all the fluxes used here.

Then, the pressure flux is

$$(\tilde{p}_{k,1/2})_{AUSM^+-up} = P^+_{(5)k}(M_{k,L})\Big|_{\alpha=3/16} \cdot p_L + P^-_{(5)k}(M_{k,R})\Big|_{\alpha=3/16} \cdot p_R + p_{uk}, \quad (2.13i)$$

$$P^\pm_{(5)}(M)\Big|_\alpha = \begin{cases} \frac{1}{2}(1 \pm sign(M)), & \text{if } |M| \geq 1, \\ \frac{1}{4}(M \pm 1)^2 (2 \mp M) \pm \alpha M (M^2 - 1)^2, & \text{otherwise}, \end{cases} \quad (2.13j)$$

$$p_{uk} = -K_u \cdot P^+_{(5)k}(M_{k,L})\Big|_{3/16} \cdot P^-_{(5)k}(M_{k,R})\Big|_{3/16} \cdot \bar{\rho}_k f_a a_{1/2} \left(V_{k,n}{}^- - V_{k,n}{}^+\right), \quad (2.13k)$$

where a tunable parameter K_u, as well as K_p in Eq. (2.13d), is set as unity in the previous works [16–18].

As seen above, the differences from the single-phase version in [11] are (1) separate fluxes but common speed of sound for gas and liquid; (2) scaling function f_a is eliminated, and hence no cutoff or freestream Mach number is required, because we are dealing with transient flows only (detailed discussions are found in [13]); and (3) averaged density, rather than a summation of left and right densities, is used in Eq. (2.13k); thus, there would be equivalently a factor of 2 difference in K_u (i.e., setting a value of K_u is equivalent to setting a half of it in [11]). In this work, AUSM$^+$-up with different K_p and K_u values will be simply denoted as AUSM$^+$-up (K_p, K_u). Note that AUSM$^+$-up $(1,1)$ is the choice commonly used, and that AUSM$^+$-up $(0, 0)$ corresponds to AUSM$^+$ [22], the version prior to AUSM$^+$-up, having no low-speed treatment. As already concluded in [16–18,20], because AUSM$^+$ lacks pressure-velocity coupling, producing oscillations in pressure and velocity across shock and contact discontinuities, it is not suitable for computing multiphase flows where the density difference is especially large. In this study, AUSM$^+$-up implies the original meaning [11,17] with nonvanishing values of K_p and K_u — especially in this study with two sets of values, $(K_p, K_u) = (1,1)$ and $(0.5, 0.5)$.

2.5.2 SLAU

SLAU (Simple Low-dissipation AUSM) by Shima and Kitamura [12] is also extended for the first time here for multiphase flows in the same manner as in AUSM$^+$-up. The mass flux for each fluid is given as:

$$(\dot{m}_{k,1/2})_{SLAU} = \frac{1}{2} \left\{ \rho_{k,L} \left(V_{k,nL} + |\bar{V}_{k,n}|^+\right) + \rho_{k,R} \left(V_{k,nR} - |\bar{V}_{k,n}|^-\right) - \frac{\chi_k}{a_{1/2}}(p_R - p_L) \right\}, \quad (2.14a)$$

$$|\bar{V}_{k,n}|^+ = (1 - g_k)|\bar{V}_{k,n}| + g_k|V_{k,nL}|, \quad |\bar{V}_{k,n}|^- = (1 - g_k)|\bar{V}_{k,n}| + g_k|V_{k,nR}|, \quad (2.14b)$$

$$|\bar{V}_{k,n}| = \frac{\rho_{k,L}|V_{k,nL}| + \rho_{k,R}|V_{k,nR}|}{\rho_{k,L} + \rho_{k,R}}, \quad (2.14c)$$

$$g_k = -\max[\min(M_{k,L}, 0), -1] \cdot \min[\max(M_{k,R}, 0), 1] \in [0, 1], \quad (2.14d)$$

$$\chi_k = \left(1 - \widehat{M}_k\right)^2,\tag{2.14e}$$

$$\widehat{M}_k = \min\left(1.0, \frac{1}{a_{1/2}}\sqrt{\frac{\mathbf{u}_{k,L}^2 + \mathbf{u}_{k,R}^2}{2}}\right),\tag{2.14f}$$

$$M_k = \frac{V_{k,n}}{a_{1/2}} = \frac{u_k n_x + v_k n_y}{a_{1/2}},\tag{2.14g}$$

where the common speed of sound for gas and liquid $a_{1/2}$ is given again by Eqs. (2.13g)-(2.13h), and the pressure flux is

$$(\tilde{p}_{k,1/2})_{SLAU} = \frac{p_L + p_R}{2} + \frac{\left.P_{(5)k}^+(M_{k,L})\right|_{\alpha=0} - \left.P_{(5)k}^-(M_{k,R})\right|_{\alpha=0}}{2}(p_L - p_R)$$
$$+ (1 - \chi_k)\left(\left.P_{(5)k}^+(M_{k,L})\right|_{\alpha=0} + \left.P_{(5)k}^-(M_{k,R})\right|_{\alpha=0} - 1\right)\frac{p_L + p_R}{2},\tag{2.14h}$$

where the function $P_{(5)}^\pm(M)$ is given by Eq. (2.13j) but with $\alpha = 0$.

The dissipation term (last term) in pressure flux had been originally designed only for the ideal gas, according to the relation $\overline{p} \propto \overline{\rho a}^2$. This term was then modified later in SLAU2 so that real fluids are treated in a unified manner.

2.5.3   SLAU2 and AUSM$^+$-up2

In SLAU2 [15], the dissipation term in the pressure flux of SLAU Eq. (2.14h) is modified as:

$$(\tilde{p}_{k,1/2})_{SLAU} = \frac{p_L + p_R}{2} + \frac{\left.P_{(5)k}^+(M_{k,L})\right|_{\alpha=0} - \left.P_{(5)k}^-(M_{k,R})\right|_{\alpha=0}}{2}(p_L - p_R)$$
$$+ \sqrt{\frac{\mathbf{u}_{k,L}^2 + \mathbf{u}_{k,R}^2}{2}}\left(\left.P_{(5)k}^+(M_{k,L})\right|_{\alpha=0} + \left.P_{(5)k}^-(M_{k,R})\right|_{\alpha=0} - 1\right)\bar{\rho}_k a_{1/2}\tag{2.15}$$

for (1) readily extending to real fluids and (2) γ times dissipation added at subsonic and more with stronger shocks. If the pressure flux of AUSM$^+$-up in Eqs. (2.13i)-(2.13k) is replaced with Eq. (2.15), AUSM$^+$-up2 [23] is realized (in this study, $K_p = 1$ is chosen). In both flux functions, the same common speed of sound Eq. (2.13g) as in AUSM$^+$-up and SLAU again stays here.

2.5.4   AUSMPW+

Kim et al. [24] proposed AUSMPW+, featuring pressure-based weighting functions with multidimensional dissipation. Instead of Eq. (2.12a), it is expressed as:

$$\mathbf{F}_{k,1/2,L/R} = \bar{M}_{k,L}^+ a_{1/2}\mathbf{\Psi}_{k,L} + \bar{M}_{k,R}^- a_{1/2}\mathbf{\Psi}_{k,R} + \alpha_{k,1/2,L/R}\tilde{p}_{k,1/2}\mathbf{N},\tag{2.16a}$$

where

for $M_{k,1/2} \geq 0$,

$$\bar{M}_{k,L}^+ = \left(M_{k,L}^+\right)_{AUSMPW+} + \left(M_{k,R}^-\right)_{AUSMPW+} \cdot [(1-\omega)\cdot(1+f_{k,R}) - f_{k,L}],$$

$$\bar{M}_{k,R}^- = \left(M_{k,R}^-\right)_{AUSMPW+} \cdot \omega \cdot (1+f_{k,R}) \tag{2.16b}$$

and for $M_{k,1/2} < 0$,

$$\bar{M}_{k,L}^+ = \left(M_{k,L}^+\right)_{AUSMPW+} \cdot \omega \cdot (1+f_{k,L}),$$

$$\bar{M}_{k,R}^- = \left(M_{k,R}^-\right)_{AUSMPW+} + \left(M_{k,L}^+\right)_{AUSMPW+} \cdot [(1-\omega)\cdot(1+f_{k,L}) - f_{k,R}]. \tag{2.16c}$$

The pressure-based weighting functions are given by:

$$\omega = 1 - \Pi_{1/2}^3, \qquad \Pi_{1/2} = \min\left(\frac{p_L}{p_R}, \frac{p_R}{p_L}\right), \tag{2.16d}$$

$$f_{k,L,R} = \begin{cases} \left(\frac{\bar{p}_{k,L,R}}{\bar{p}_{k,s}} - 1\right) \cdot \min\left(1, \frac{\min(\bar{p}_{k,L,1}, \bar{p}_{k,R,1}, \bar{p}_{k,L,2}, \bar{p}_{k,R,2})}{\min(\bar{p}_{k,L}, \bar{p}_{k,R})}\right)^2 & \text{if } p_s \neq 0, \\ 0 & \text{if } p_s = 0, \end{cases} \tag{2.16e}$$

$$\bar{p}_k = p_k + p_{k\infty}, \qquad \bar{p}_{k,s} = \tilde{p}_{k,1/2} + p_{k\infty}, \tag{2.16f}$$

where $p_{L,1}$ and $p_{L,2}$, and $p_{R,1}$ and $p_{R,2}$ are pressure at neighboring cells of "L" and "R," respectively, in the direction tangent to the cell interface between "L" and "R" in 2D. Note that one of the two weight functions, ω, is common to both gas and liquid, while the other, $f_{k,L,R}$, is defined differently according to the EOS of each phase, as suggested very recently by Park and Kim [49]. We point out here that without this modification to the liquid phase, this flux failed in most of the problems treated in the present paper, as demonstrated in our earlier work [50].

The mass flux is then written as:

$$(M_{k,1/2})_{AUSMPW+} = \left.M_{(4)k}^+ (M_{k,L})\right|_{\beta=0} + \left.M_{(4)k}^- (M_{k,R})\right|_{\beta=0}, \tag{2.16g}$$

where the function $M_{(4)}^{\pm}(M)$ is given by Eq. (2.13c) with $\beta = 0$, and the pressure flux is given by Eq. (2.13i). The speed of sound for each phase is defined using the cell-interface-normal component of the total enthalpy for this flux:

$$(a_{k,1/2})_{AUSMPW+} = \begin{cases} a_{k,s}^2 / \max(|V_{k,nL}|, a_{k,s}), & \text{if } V_{k,nL} + V_{k,nR} \geq 0, \\ a_{k,s}^2 / \max(|V_{k,nR}|, a_{k,s}), & \text{if } V_{k,nL} + V_{k,nR} < 0, \end{cases} \tag{2.16h}$$

$$a_{k,s} = \sqrt{2H_{k,n}(\gamma_k - 1)/(\gamma_k + 1)}, \tag{2.16i}$$

$$H_{k,n} = \frac{1}{2}\left(H_{k,L} - \frac{V_{k,tL}^2}{2} + H_{k,R} - \frac{V_{k,tR}^2}{2}\right), \tag{2.16j}$$

(a)   (b)
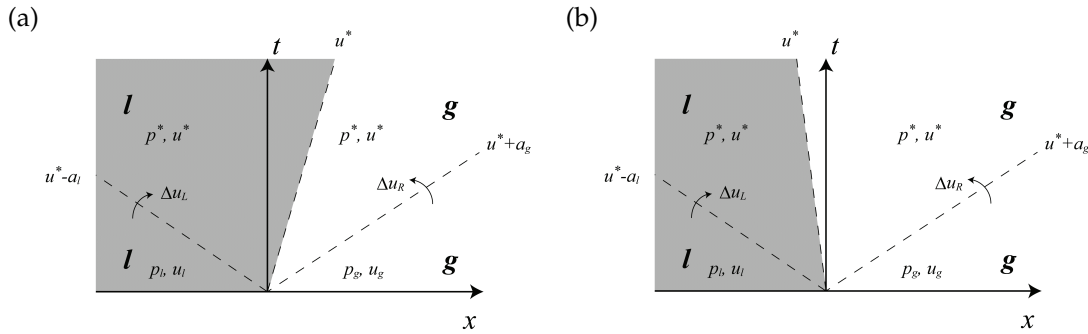
Figure 4: Illustration of Riemann problem for liquid (l) and gas (g) interface, (a) Liquid flows into gas; (b) Gas flows into liquid.

where the subscript n denotes the normal component, and t the tangential one. Then, the gas and liquid speed of sound are averaged arithmetically as the final value:

$$a_{1/2} = \frac{1}{2}\left(a_{l,1/2} + a_{g,1/2}\right).$$

A variation of this flux was published by Ihm and Kim in [35] for one-fluid, two-phase flow extension with some success. Since their modifications involve many mixture variables (e.g., mixture density) that are absent in two-fluid modeling, it is not applied in this study.

2.5.5   G-AUSM$^+$-up, G-SLAU2, and G-AUSMPW+: Combinations with the Exact Riemann (Godunov) Solver

As stated in Introduction, making use of the exact Riemann (Godunov) solver is another approach (Group 2). In practice, the Godunov solver is used only when the void fraction jump (or the "effective length", $\Delta_{eff} = |\alpha_{g,1/2,L} - \alpha_{g,1/2,R}|$) is larger than the prescribed threshold, or ε (Fig. 2c); otherwise, only an AUSM-family scheme is used (Group 1, Fig. 2b). In other words, Group 2 includes Group 1 in cases of small effective length (Fig. 2d).

The exact Riemann (Godunov) solver [25] for stiffened-gas EOS is written in a very similar manner as in the ideal gas [17,51]. For instance, if the liquid phase is at the left side and the gas is at the right (i.e., $\alpha_{g,1/2,L} + \varepsilon < \alpha_{g,1/2,R}$) as in Fig. 2c, or in Fig. 4 of x-t diagram (a more common way to illustrate a Riemann problem),

1) First, the middle zone pressure p^* is estimated, such as $p^* = 0.5(p_l + p_g)$.

2) If $p^* > p_l$, the left-running wave "$u-a$" is assumed to be a shock wave, and hence, the velocity jump Δu_L across it is given by

$$\Delta u_L = (p^* - p_l)\left[\frac{2}{\rho_l\left((\gamma_l+1)[p^*+p_{l\infty}] + (\gamma_l-1)[p_l+p_{l\infty}]\right)}\right]^{1/2}. \qquad (2.17a)$$

Otherwise, the expansion waves should be there, resulting in the velocity difference Δu_R by the isentropic relation:

$$\Delta u_L = \frac{2a_l}{\gamma_l - 1} \left[(\xi_l)^{\frac{\gamma_l - 1}{2\gamma_l}} - 1 \right] \tag{2.17b}$$

with

$$\xi_l = \frac{p^* + p_{l\infty}}{p_l + p_{l\infty}}. \tag{2.17c}$$

3) Similarly, if $p^* > p_R$, the right-running wave "$u+a$" is a shock, and the velocity jump Δu_R is:

$$\Delta u_R = (p^* - p_g) \left[\frac{2}{\rho_g \left((\gamma_g + 1) p^* + (\gamma_g - 1) p_g \right)} \right]^{1/2}. \tag{2.17d}$$

Otherwise,

$$\Delta u_R = \frac{2a_g}{\gamma_g - 1} \left[(\xi_g)^{\frac{\gamma_g - 1}{2\gamma_g}} - 1 \right], \tag{2.17e}$$

where

$$\xi_g = \frac{p^*}{p_g}. \tag{2.17f}$$

4) Since $u^* = u_l - \Delta u_L$ and $u^* = u_g + \Delta u_R$, the following should be satisfied:

$$f^* \equiv u_g + \Delta u_R - u_l + \Delta u_L = 0. \tag{2.17g}$$

If $|f^*|$ is above the specified tolerance (10^{-4}, in this study), the middle zone pressure p^* is updated as:

$$\begin{aligned}
(p^*)^{m+1} &= (p^*)^m - \frac{f^*}{\partial f^* / \partial (p^*)^m} \\
&= (p^*)^m - \frac{f^*}{\partial (\Delta u_R) / \partial (p^*)^m + \partial (\Delta u_L) / \partial (p^*)^m},
\end{aligned} \tag{2.17h}$$

where m is the Newton iteration stage, and the procedure 2) - 4) is repeated until the tolerance is satisfied.

5) Once the f^* is obtained, the other middle zone variables are calculated as:

$$u^* \equiv 0.5 \left(u_g + \Delta u_R + u_l - \Delta u_L \right), \tag{2.17i}$$

$$\rho_l^* = \begin{cases} \rho_l \left(\frac{\theta_l \xi_l + 1}{\theta_l + \xi_l} \right) & \text{if } p^* > p_l, \\ \rho_l (\xi_l)^{1/\gamma_l} & \text{otherwise,} \end{cases} \tag{2.17j}$$

$$\rho_g^* = \begin{cases} \rho_g \left(\frac{\theta_g \xi_g + 1}{\theta_g + \xi_g} \right) & \text{if } p^* > p_g, \\ \rho_g (\xi_g)^{1/\gamma_g} & \text{otherwise,} \end{cases} \tag{2.17k}$$

with

$$\theta_k = \frac{\gamma_k + 1}{\gamma_k - 1}. \tag{2.17l}$$

6) If $u^* > 0$, the liquid (left) flows into the gas (right) at the interface (Fig. 4a), and thus, the liquid flux is given as:

$$\mathbf{F}_{l-g,1/2-Godunov} = \Delta_{eff} \cdot \begin{bmatrix} \rho_l^* u^* & \rho_l^* u^{*2} & \rho_l^* u^* v_l & \rho_l^* u^* & h_l^* \end{bmatrix}, \tag{2.17m}$$

where

$$h_l^* = \frac{\gamma_l}{\gamma_l - 1} \frac{p^* + p_{l\infty}}{\rho_l^*} + \frac{1}{2}\left(u^{*2} + v_l^2\right) \tag{2.17n}$$

and otherwise, the gas (right) phase comes into the liquid (left) (Fig. 4b) as

$$\mathbf{F}_{l-g,1/2-Godunov} = \Delta_{eff} \cdot \begin{bmatrix} \rho_g^* u^* & \rho_g^* u^{*2} & \rho_g^* u^* v_g & \rho_g^* u^* & h_g^* \end{bmatrix}^T, \tag{2.17o}$$

where

$$h_g^* = \frac{\gamma_g}{\gamma_g - 1} \frac{p^*}{\rho_g^*} + \frac{1}{2}\left(u^{*2} + v_g^2\right). \tag{2.17p}$$

7) Furthermore, interface pressure flux is also applied as in Eq. (2.7),

$$p^{int} = p^* - \sigma \frac{\alpha_g^{int} \alpha_l^{int} \rho_g \rho_l}{\alpha_g^{int} \rho_l + \alpha_l^{int} \rho_g} \left| \mathbf{u}_l - \mathbf{u}_g \right|^2, \tag{2.17q}$$

where $\sigma = 2.0$, the Eq. (2.9) is again applied to the second term at the right hand side, and

$$\alpha_g^{int} = 0.5\left(\alpha_{g,1/2,L} + \alpha_{g,1/2,R}\right); \qquad \alpha_l^{int} = 1 - \alpha_g^{int}. \tag{2.17r}$$

Again, the Godunov solver is used at gas (left)-liquid (right) or liquid (left)-gas (right) interfaces only; gas-gas and liquid-liquid interfaces are treated by a selected AUSM-family scheme. Thus, the flux of the AUSM-family portion is calculated according to Eq. (2.12), but with the modification of $\alpha_{k,1/2,L/R}$ to $\min(\alpha_{k,1/2,L}, \alpha_{k,1/2,R})$ so that the common and minimum void fraction of both sides is used and the room for Godunov solver $\Delta_{eff} = |\alpha_{g,1/2,L} - \alpha_{g,1/2,R}|$ is left, in contrast to the Group 1. Therefore, the resulting flux is expressed as summation of gas-gas part (AUSM-family), liquid-liquid part (AUSM-family), and liquid-gas part (Godunov) (again,

if $\alpha_{g,1/2,L}+\varepsilon<\alpha_{g,1/2,R}$), as illustrated in Fig. 2c.

$$
\left.
\begin{aligned}
\mathbf{F}_{l,1/2,L} &= \mathbf{F}_{l,1/2-AUSM-family}+\mathbf{F}_{l-g,1/2-Godunov}+\Delta_{eff}\cdot p^{\mathrm{int}}\\
\mathbf{F}_{g,1/2,L} &= \mathbf{F}_{g,1/2-AUSM-family}\\
\mathbf{F}_{l,1/2,R} &= \mathbf{F}_{l,1/2-AUSM-family}+\mathbf{F}_{l-g,1/2-Godunov}\\
\mathbf{F}_{g,1/2,R} &= \mathbf{F}_{g,1/2-AUSM-family}+\Delta_{eff}\cdot p^{\mathrm{int}}
\end{aligned}
\right\}\ \text{if } u^*>0,
$$

$$
\left.
\begin{aligned}
\mathbf{F}_{l,1/2,L} &= \mathbf{F}_{l,1/2-AUSM-family}+\Delta_{eff}\cdot p^{\mathrm{int}}\\
\mathbf{F}_{g,1/2,L} &= \mathbf{F}_{g,1/2-AUSM-family}+\mathbf{F}_{l-g,1/2-Godunov}\\
\mathbf{F}_{l,1/2,R} &= \mathbf{F}_{l,1/2-AUSM-family}\\
\mathbf{F}_{g,1/2,R} &= \mathbf{F}_{g,1/2-AUSM-family}+\mathbf{F}_{l-g,1/2-Godunov}+\Delta_{eff}\cdot p^{\mathrm{int}}
\end{aligned}
\right\}\ \text{otherwise.}\quad (2.17s)
$$

In the case of a gas (left)-liquid (right) interface, L and R are flipped over. In addition, for the AUSM-family portion in Group 2, Eq. (2.13g) for the gas-liquid-averaged acoustic speed is not used for AUSM-family schemes because each phase is computed totally independently. The combination of Godunov and AUSM$^+$-up (1, 1) [17] is denoted as "G-AUSM$^+$-up (1, 1)" here, for example. Likewise, the newly-extended "G-SLAU", "G-SLAU2", "G-AUSM$^+$-up2", and "G-AUSMPW+" are possible. In this work, only G-AUSM$^+$-up (1, 1), G-SLAU2, and G-AUSMPW+ are compared.

2.6 Time integration, decoding, and update of variables

Equation (2.6) is rewritten in the three-stage TVD Runge-Kutta [45] form as:

$$
\hat{\mathbf{Q}}_j^{(1)}=\hat{\mathbf{Q}}_j^n+\frac{\Delta t}{V_j}\mathbf{R}_j^n, \tag{2.18a}
$$

$$
\hat{\mathbf{Q}}_j^{(2)}=\frac{3}{4}\hat{\mathbf{Q}}_j^n+\frac{1}{4}\hat{\mathbf{Q}}_j^{(1)}+\frac{1}{4}\frac{\Delta t}{V_j}\mathbf{R}_j^{(1)}, \tag{2.18b}
$$

$$
\hat{\mathbf{Q}}_j^{n+1}=\frac{1}{3}\hat{\mathbf{Q}}_j^n+\frac{2}{3}\hat{\mathbf{Q}}_j^{(2)}+\frac{2}{3}\frac{\Delta t}{V_j}\mathbf{R}_j^{(2)}, \tag{2.18c}
$$

$$
\hat{\mathbf{Q}}_j\equiv\mathbf{Q}_j+\begin{bmatrix}0\\0\\p_j^{\mathrm{int}}\alpha_j\end{bmatrix}=\begin{bmatrix}\hat{Q}_1\\\hat{Q}_2\\\hat{Q}_3\end{bmatrix}, \tag{2.18d}
$$

$$
\mathbf{R}_j\equiv-\left[\mathbf{E}_{j+1/2}S_{j+1/2}-\mathbf{E}_{j-1/2}S_{j-1/2}\right]+\begin{bmatrix}0\\p_j^{\mathrm{int}}\left(\alpha_{j+1/2,L}-\alpha_{j-1/2,R}\right)\\0\end{bmatrix}+\mathbf{S}_j, \tag{2.18e}
$$

where k is omitted, and the term $(p^{\mathrm{int}}\alpha)$ is included in $\hat{\mathbf{Q}}$ as in Eq. (2.18d) [16, 19], but p^{int} is frozen at the nth time step value throughout the Runge-Kutta stages [19].

Once $\widehat{\mathbf{Q}}^{n+1}$ is obtained, the following decoding process is required to update p^{n+1} and α_k^{n+1} by solving p^{n+1} from

$$
F(p)=p^2-Bp-C=0. \tag{2.19}
$$

Since p is positive, a unique root is determined:

$$p = \frac{1}{2}\left(B + \sqrt{B^2 + 4C}\right) \tag{2.20a}$$

and the volume fraction follows:

$$\alpha_k = \frac{\hat{A}_k}{p + \hat{a}_k}, \tag{2.20b}$$

where

$$\hat{A}_k = (\gamma_k - 1)\left(\hat{Q}_{3,k} - \frac{\hat{Q}_{2,k}^2}{2\hat{Q}_{1,k}}\right), \tag{2.20c}$$

$$B = \sum_{k=1}^{2}\left(\hat{A}_k - \hat{a}_k\right), \tag{2.20d}$$

$$C = \hat{a}_1 \hat{A}_2 + \hat{a}_2 \hat{A}_1 - \hat{a}_1 \hat{a}_2, \tag{2.20e}$$

$$\hat{a}_k = \gamma_k p_{k,\infty} + (\gamma_k - 1)p^{\text{int}}. \tag{2.20f}$$

Since a huge value of $p_{l\infty}$ is involved in Eqs. (2.18) and (2.20), the resultant numerical errors can be large. Thus, a Newton iteration method is introduced to improve accuracy by solving Eq. (2.20b) simultaneously for both the liquid and gas phases [17]:

$$\begin{cases} F_g = (p + \hat{a}_g)\alpha_g - \hat{A}_g = 0, \\ F_l = (p + \hat{a}_l)\alpha_l - \hat{A}_l = 0. \end{cases} \tag{2.21}$$

Usually, a few iterations are enough to drive pressure error below 10^{-5}.

Then, following Paillère et al. [20] and Chang and Liou [17], variables of the "vanishing" phase (i.e., $\varepsilon_{\min} \leq \alpha_1 \leq \varepsilon_{\max}$) are blended with those of the remaining phase (i.e., $\alpha_2 \approx 1$) to enhance stability:

$$(q_1)_{adjust} = G(\xi_1)q_1 + (1 - G(\xi_1))q_2, \quad q = \mathbf{u}, T, \tag{2.22a}$$

$$G(\xi_1) = -\xi_1^2(2\xi_1 - 3), \tag{2.22b}$$

$$\xi_1 = \frac{\alpha_1 - \varepsilon_{\min}}{\varepsilon_{\max} - \varepsilon_{\min}}, \tag{2.22c}$$

where G is a smooth function satisfying $G(0) = 0$, $G(1) = 1$, and $G'(0) = G'(1) = 0$. The small values of $\varepsilon_{\min}$ and $\varepsilon_{\max}$ are chosen as $0.1\varepsilon(=10^{-8})$ and $10^3\varepsilon(=10^{-4})$ in this paper, if not mentioned otherwise. If α_1 is below $\varepsilon_{\min}$, $\alpha_1 = \varepsilon_{\min}$ is enforced. Here $k = 1,2$ is interchangeable with $k = g,l$ and $k = l,g$ both. We must update $(\mathbf{u}, T)$, not $(\mathbf{u}, \rho)$. If the density is replaced by that of the other phase, which differs by a factor of $\mathcal{O}(10^3)$, possibly resulting in a huge error in water temperature, say, $\mathcal{O}(10^5)$ [K] at the standard sea-level conditions.

2.7   Boundary conditions

Since a cell-centered, 2D structured grid solver is used here, the following typical boundary conditions using the typical "ghost cell" approach are applied as in [20]:

- Inlet: all the variables are imposed except for pressure, which is extrapolated from the interior cell.
- Outlet: only pressure is imposed, and all the other variables are extrapolated from the interior cell.
- Side (for a 1D problem): all the variables are extrapolated from the interior cell (for the direction irrelevant to the problem to be solved).
- Slip: also known as "mirror" condition, in which the opposite sign is put to the velocity component normal to the boundary, and all the other variables are extrapolated from the interior cell.

3   Numerical examples

In what follows, we shall demonstrate that the recently developed AUSM-family fluxes — AUSM$^+$-up (1, 1), AUSM$^+$-up (0.5, 0.5), SLAU, SLAU2, AUSM$^+$-up2, and AUSMPW+ — are extended to multiphase flows in the same framework, and compare their performances. For ease of reference, all the results will be summarized in Tables 1 and 2 later in this section. The results of AUSM$^+$-up (0, 0), known to fail to yield stable solutions [16], are thus not included. The grid study is performed for AUSM$^+$-up (0.5, 0.5), which will display the middle diffusivity/smoothness in most tests (the other schemes behave in similar manners), and selected results are shown in Subsections 3.2 Faucet Problem, 3.3.1 Air-to-Water Shock Tube, and 3.3.2 Water-to-Air Shock Tube.

In addition, the following "CFL-like number", usually taken between 0.05 and 0.63, is used to determine the time step:

$$CFL = \Delta t \bigg/ \min_j \left(\frac{\Delta x}{\max\left(a_g, a_l\right) + \max\left(|\mathbf{u}_g|, |\mathbf{u}_l|\right)} \right)_j. \tag{3.1}$$

3.1   Moving phase contact discontinuity

As the first problem, a moving contact discontinuity between air and water separated at $x = 5$ m [17] is solved. It is desired to accurately capture this phase discontinuity, across which pressure constancy should be maintained. A grid of 200 uniform cells is used for the [0 m, 10 m] domain (hence, the grid spacing $\Delta x = 0.05$ m), and the initial conditions are given as:

- $(p, \alpha_g, u_k, T_k)_L = (10^5$ Pa, $1 - \varepsilon$, 100 m/s, 300 K) for $x \leq 5$ m;
- $(p, \alpha_g, u_k, T_k)_R = (10^5$ Pa, ε, 100 m/s, 300 K) for $x > 5$ m,

where $k = g, l$, and $\varepsilon = 1.0 \times 10^{-7}$ ($\varepsilon_{min} = 1.0 \times 10^{-8}$, $\varepsilon_{max} = 1.0 \times 10^{-4}$). Note that this setup leads to $\rho_l = 1053$ kg/m^3 and $\rho_g = 1.16$ kg/m^3; that is, a large density ratio of $\mathcal{O}(10^3)$ across the interface, which is known to be a tough condition for preserving a constant pressure, say within an $\mathcal{O}(10^{-3})$ error [52]. The computations are conducted with $\Delta t = 6.0 \times 10^{-6}$ s (CFL ≈ 0.2), up to 0.03 s (5,000 steps).

The results are shown in Figs. 5 and 6 for Groups 1 and 2, respectively. All the fluxes tested showed excellent performance both in smooth transition of the two phases (Figs. 5a and 6a) and in preserving a uniform pressure across the contact discontinuity (Figs. 5b and 6b). When the pressure is expanded as in Figs. 5c and 6c, there are from $\mathcal{O}(10^{-6})$ to $\mathcal{O}(10^{-5})$ Pa of disturbances downstream the interface with different profiles; still, they are negligible ($\mathcal{O}(10^{-11}) - \mathcal{O}(10^{-10})$) compared with the initial uniform pressure, 10^5 Pa.

We also surveyed effects of flux limiter functions. The moving phase-discontinuity results of AUSM$^+$-up (1, 1) with the following limiters are compared: Van Albada [44] [denoted as "VA", with the limiter coefficient 10^{-20} (default) or 10^{-6}], minmod [53], or Chakravarthy-Osher [54] (denoted as "C-O", which was adopted in Chang and Liou [17]), in combination with two MUSCL coefficients $\kappa = -1$ (default; fully upwind second order) or $1/3$ (upwind-biased third order). The results are shown in Fig. 7, in which pressure disturbance is examined at the 10^{-6} Pa level. It is seen that the C-O limiter (with either $\kappa = -1$ or $1/3$) has the best performance in preserving pressure constancy, but more importantly, any choice can suppress the pressure error within 10^{-5} Pa, which is 10 orders smaller than the uniform pressure. From these results, we selected the Van Albada's limiter with $\kappa = -1$ as the default choice throughout the paper, because we found it the most robust for the challenging shock/water-column test (shown later in Subsection 3.5).

3.2 Faucet problem

The second test is the well-known "Faucet" problem suggested by Ransom [55], in which a water jet is injected at a speed of 10 m/s and accelerated by gravity downward (and hence, narrowed, according to the mass conservation law) into a stationary air, in a 12-m-long tube [0 m, 12 m]. This problem is usually modeled by the following initial conditions:

- $(p, \alpha_g, u_g, u_l, T_g, T_l) = (10^5$ Pa, 0.2, 0 m/s, 10 m/s, 300 K, 300 K$)$.

The same set is applied to the inlet boundary condition, except for the pressure, which is extrapolated from the interior cell; whereas at the outlet a pressure of 10^5 Pa is specified, and other variables are extrapolated from the immediate interior cell. Note that the gas and liquid velocities here are set to be different, as in [20, 37, 38], instead of being equal [17, 34]. It is a feature of the two-fluid model that different velocities are allowed within a single cell, in contrast to one-fluid model having only one velocity according to the velocity-equilibrium assumption [34]. Only in this test case, $(g_x, g_x) = (9.8 \text{m/s}^2, 0 \text{m/s}^2)$ is activated in the source term of Eq. (2.1b) in order to reproduce the gravity effects accelerating the water downward ($+x$-direction). The computational setup is as follows:

(a)

(a)

(b)

(b)

(c)

(c)
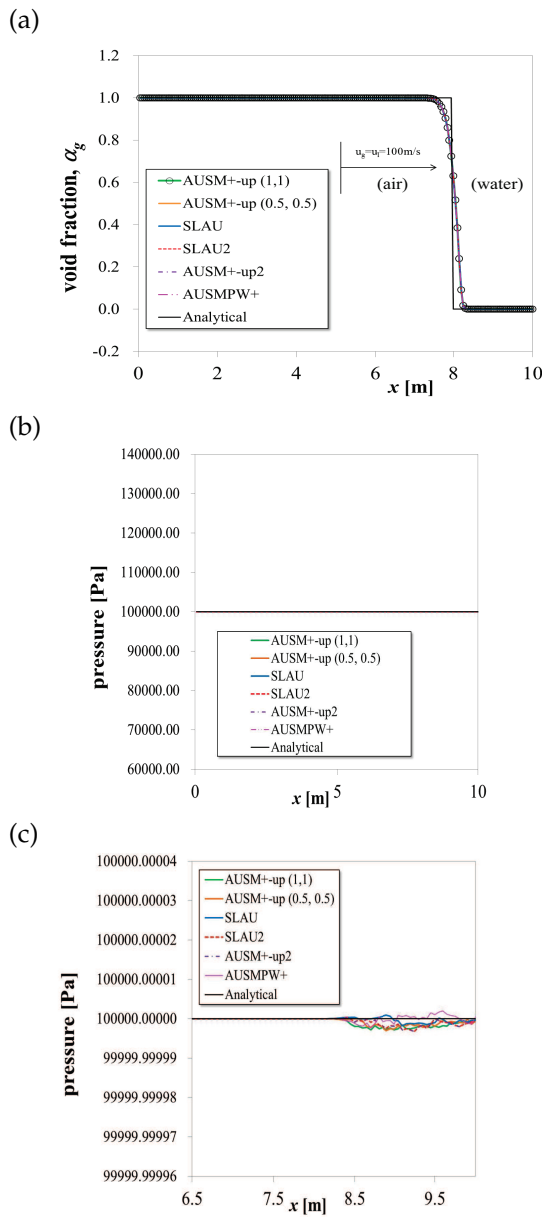
Figure 5: Moving phase-contact discontinuity solutions (Group 1) at $t=0.03$ s, (a) Void fraction, α_g; (b) Pressure; (c) Pressure (expanded scale).
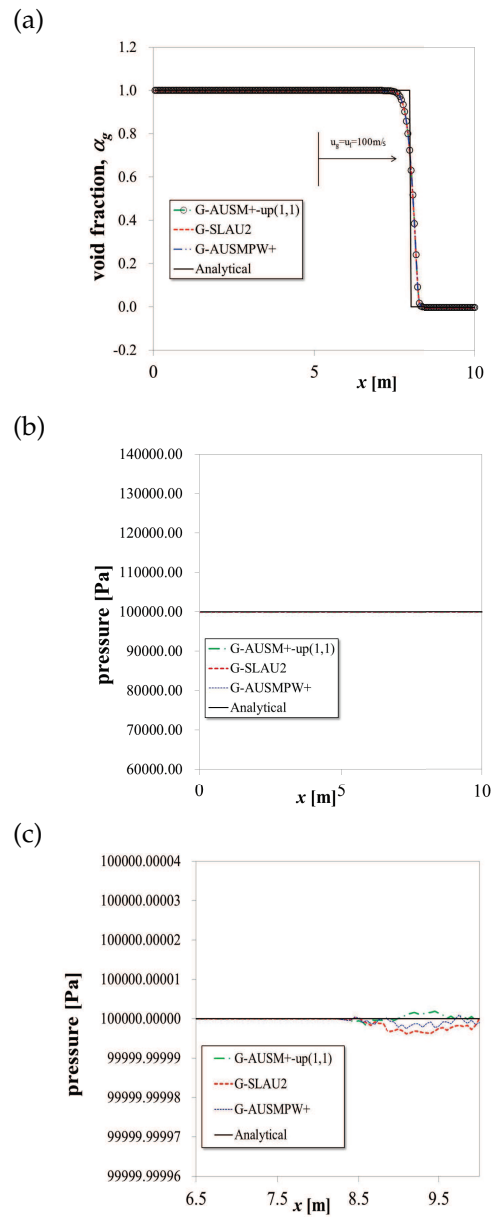
Figure 6: Moving phase-contact discontinuity solutions (Group 2) at $t=0.03$ s, (a) Void fraction, α_g; (b) Pressure; (c) Pressure (expanded scale).

- 500 cells: $\Delta x=0.024$ m, $\Delta t=1.0\times10^{-5}$s (CFL ≈0.63), computations up to 0.5 s (50,000 steps) [*default grid*].
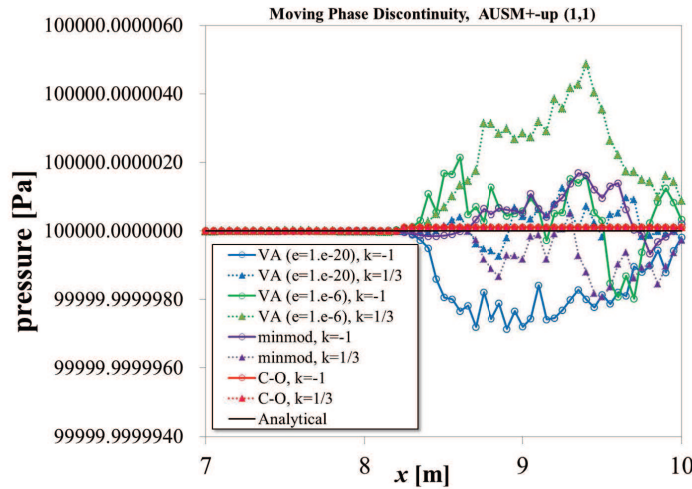
Figure 7: Effects of limiter functions on pressure disturbance from moving phase contact discontinuity.

The computed results are compared with the following analytical solution [20]:

$$
\alpha_g(x,t) = \begin{cases} 1 - \dfrac{\left(1-\alpha_g(0,0)\right)\cdot u_l(0,0)}{\sqrt{(u_l(0,0))^2 + 2g_x x}} & \text{if } x < \dfrac{gt^2}{2} + u_l(0,0)\cdot t, \\ \alpha_g(0,0) & \text{else.} \end{cases}
\tag{3.2}
$$

The results are shown in Figs. 8 and 9 in terms of void fraction profiles at 0.5 s. AUSM$^+$-up (1, 1) and (0.5, 0.5) showed slight overshoots at the top of the wave front (Fig. 8b), whereas the others exhibit slightly abrupt drop at the bottom (Fig. 8c); but in general, all the Group 1 flux functions yielded almost the same, smooth profiles without serious oscillations (Fig. 8a). In addition, when the Godunov solver is combined (Group 2), those weak oscillations are smoothed out (Fig. 9), although G-AUSM$^+$-up (1, 1) still showed a very slight overshoot (Fig. 9b).

In order to see the grid effects, this problem is solved with two more different grids:

- 1,000 cells: $\Delta x = 0.012$ m, $\Delta t = 5.0 \times 10^{-6}$ (CFL ≈ 0.63), computations up to 0.5 s (100,000 steps) [*fine grid*];

- 2,000 cells: $\Delta x = 0.006$ m, $\Delta t = 2.5 \times 10^{-6}$ (CFL ≈ 0.63), computations up to 0.5 s (200,000 steps) [*very fine grid*].

As shown in Fig. 10, grid convergence is achieved with smooth profile: as the grid points increase, the numerical solution approaches the analytical one.

We can say that all the methods have successfully computed the above two multi-phase flows with satisfactory results. In the next examples, steep pressure gradients will appear and affect the solutions noticeably.
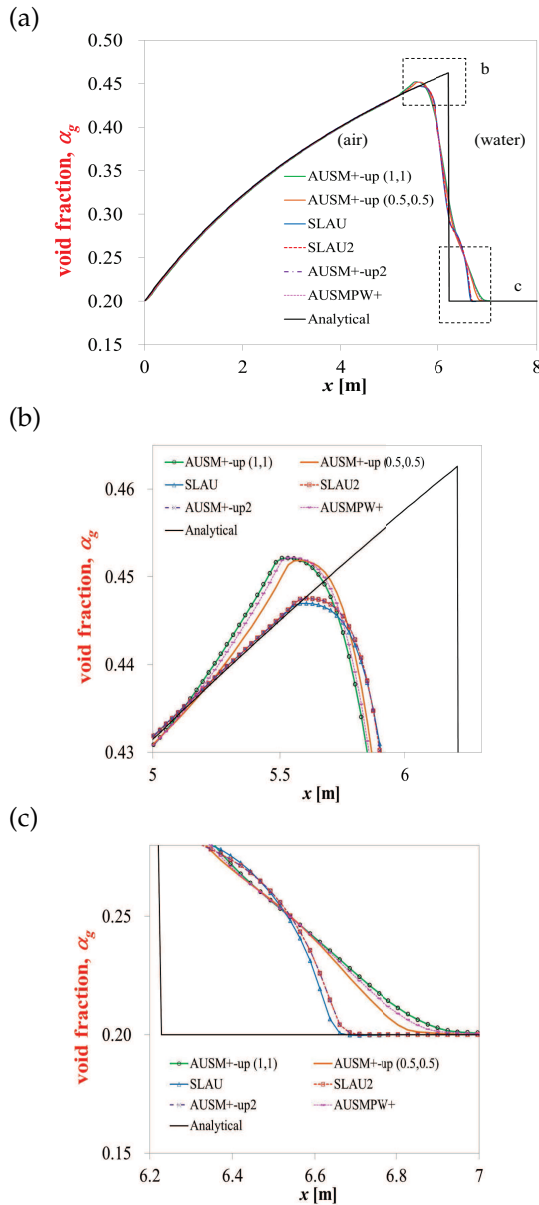
Figure 8: Faucet problem solutions (Group 1) at $t=0.5$ s, (a) Overview; (b) Expanded view of top of wave front; (c) Expanded view of bottom of wave front.
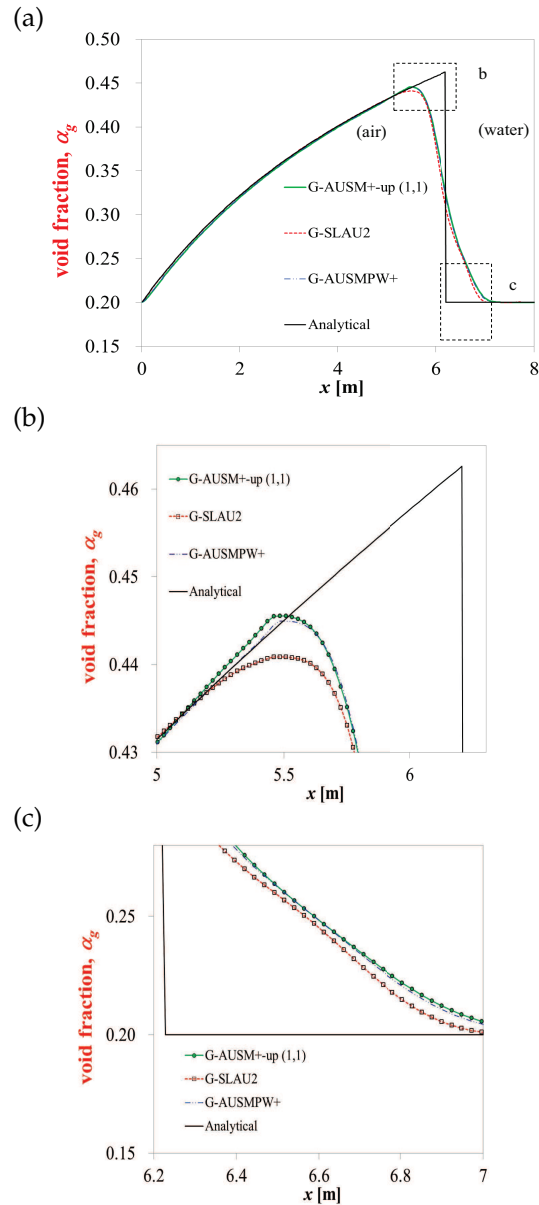
Figure 9: Faucet problem solutions (Group 2) at $t=0.5$ s (a) Overview; (b) Expanded view of top of wave front; (c) Expanded view of bottom of wave front.

3.3 Shock tube problems

3.3.1 Air-to-Water shock tube

As in the moving contact discontinuity problem, a 1D domain [0 m, 10 m] is separated by left and right states at $x=5$ m, but with the following different conditions:
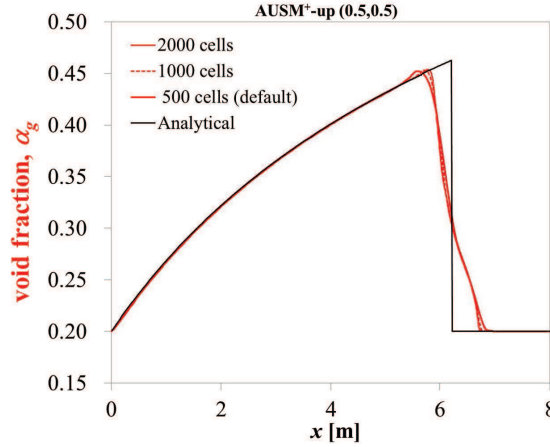
Figure 10: Faucet problem solutions of different grids at $t=0.5$ s, AUSM$^+$-up (0.5, 0.5).

- $(p,\alpha_g,u_k,T_k)_L = (10^9 \text{ Pa}, 1-\varepsilon, 0 \text{ m/s}, 308.15 \text{ K})$ for $x \leq 5$ m;
- $(p,\alpha_g,u_k,T_k)_R = (10^5 \text{ Pa}, \varepsilon, 0 \text{ m/s}, 308.15 \text{ K})$ for $x > 5$ m,

where $k=g,l$, and $\varepsilon = 1.0 \times 10^{-7}$ ($\varepsilon_{\min} = 1.0 \times 10^{-8}$, $\varepsilon_{\max} = 1.0 \times 10^{-4}$). A grid composed of the following uniform cells with time step is used:

- 500 cells: $\Delta x = 0.02$ m, $\Delta t = 2.0 \times 10^{-6}$ s (CFL ≈ 0.2), computed up to 2.0×10^{-3} s (1,000 steps) [*default grid*].

The results represented by AUSM$^+$-up (1, 1) and G-AUSM$^+$-up (1, 1) are shown in Fig. 11. All the cases displayed smoothly captured a rarefaction wave in air ($x \approx 4.5$ m), a phase interface between air and water ($x \approx 5.5$ m), and a shock in water ($x \approx 8.5$ m). This is clearly seen in the magnified view of the top of the shock front in Fig. 12a, in which all the Group 1 results are compared: AUSM$^+$-up (1, 1), AUSM$^+$-up (0.5, 0.5), SLAU2, and AUSM$^+$-up2 are smooth (with this order of smoothness), of which the last two sharing the common pressure flux give indistinguishable results. SLAU and AUSMPW+ showed a slight kink due to a smaller dissipation than in others. In Group 2 (Fig. 12b), only G-AUSMPW+ showed slight pressure oscillations that are absent in G-AUSM$^+$-up (1, 1) or G-SLAU2. This is not surprising, because at this place nearly pure water is treated (i.e., no phase interface), and hence, the exact Riemann solver is not called; the slight difference from AUSMPW+ result comes at the beginning of the computation when even this small water shock wave was recognized to include a phase discontinuity, $\Delta_{eff} = |\alpha_{g,1/2,L} - \alpha_{g,1/2,R}| > \varepsilon$.

The second grid study solved this air-to-water shock tube test, with the following grid:

- 5,000 cells: $\Delta x = 0.002$ m, $\Delta t = 2.0 \times 10^{-7}$ s (CFL ≈ 0.2), computed up to 2.0×10^{-3} s (10,000 steps) [*fine grid*].

The results are summarized in Fig. 13, again showing grid convergence for each variable.
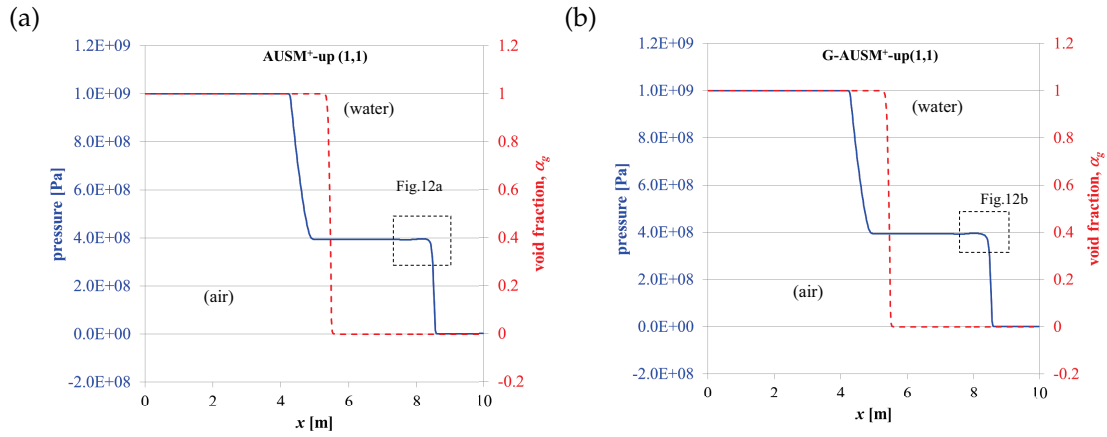
Figure 11: Air-to-water shock tube problem solutions at $t=2$ ms, (a) AUSM$^+$-up (1, 1) (representing Group 1); (b) G-AUSM$^+$-up (1, 1) (representing Group 2).
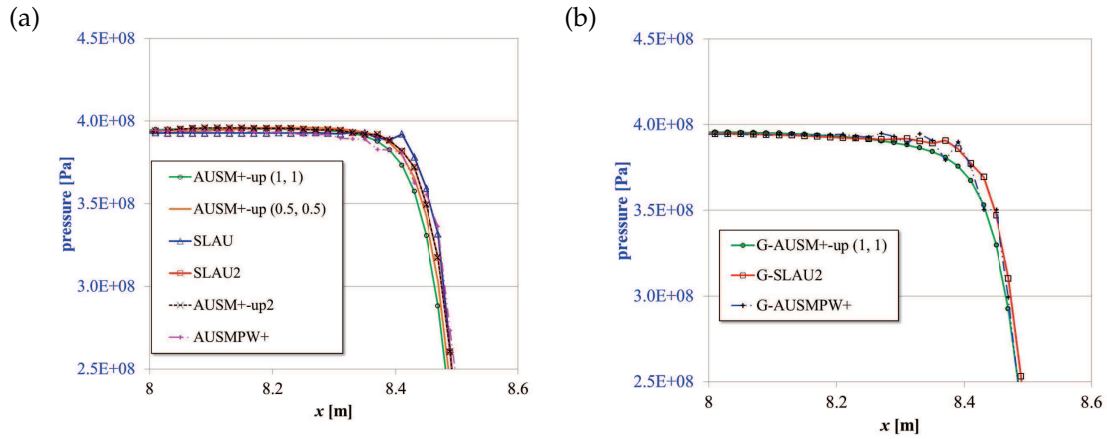

Figure 12: Magnified view of pressure profiles near shock front in water at $t=2$ ms of the air-to-water shock tube problem, (a) Group 1; (b) Group 2.

3.3.2 Water-to-Air shock tube

Now the same grid system is used as in the air-to-water shock tube with the following setup:

- $(p,\alpha_g,u_k,T_k)_L=(1\times10^7 \text{ Pa}, \varepsilon, 0 \text{ m/s}, 308.15 \text{ K})$ for $x\leq5$ m;
- $(p,\alpha_g,u_k,T_k)_R=(5\times10^6 \text{ Pa}, 1-\varepsilon, 0 \text{ m/s}, 308.15 \text{ K})$ for $x>5$ m,

with the following grid and time step:

- 500 cells: $\Delta x=0.02$ m, $\Delta t=2.0\times10^{-6}$ s (CFL ≈0.2), computed up to 2.0×10^{-3} s (1,000 steps) [*Default Grid*].

(a)

(b)

(c)

(d)
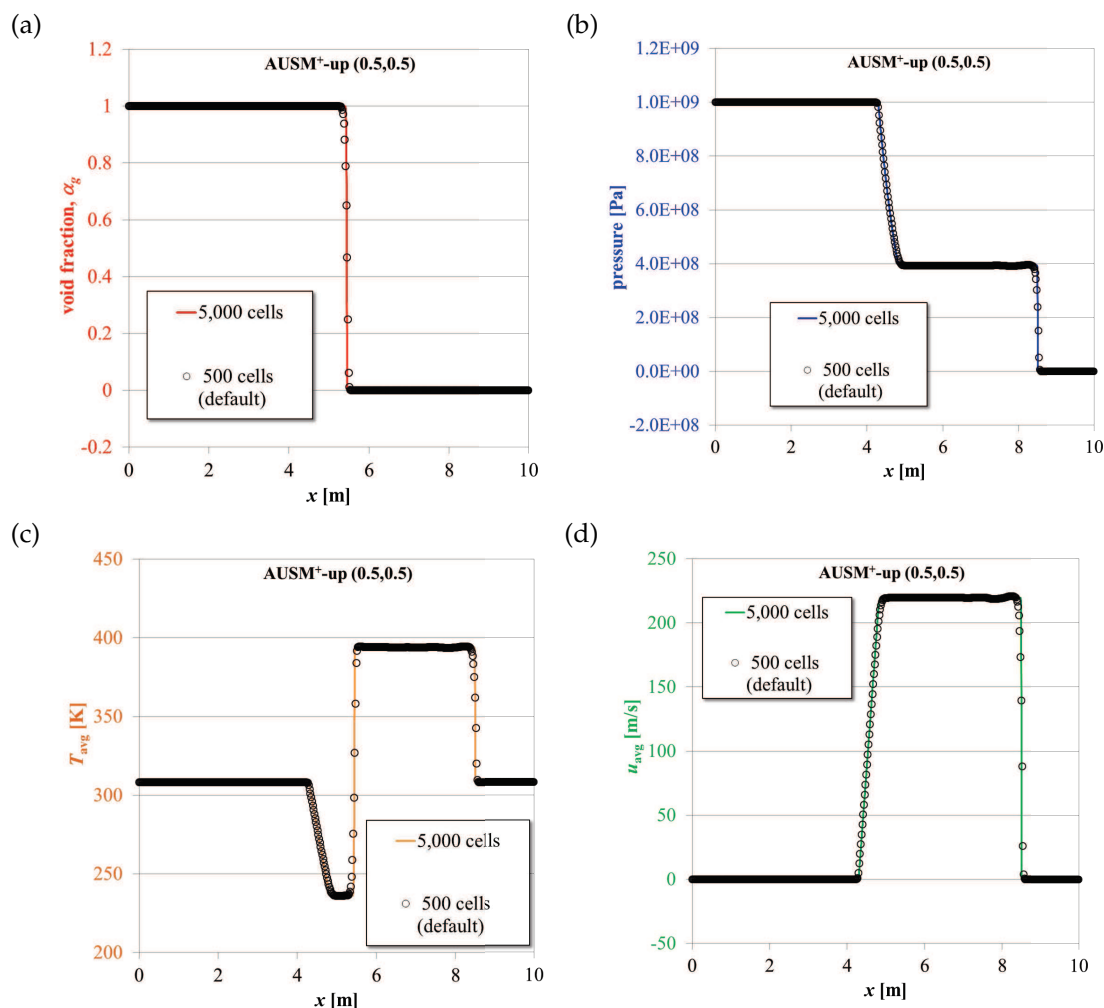
Figure 13: Solutions showing grid convergence at $t=2$ ms of the air-to-water shock tube problem of AUSM$^+$-up (0.5, 0.5), (a) Void fraction; (b) Pressure; (c) Average temperature; (d) Average velocity.

The results for AUSM$^+$-up (1, 1) representing Group 1 are shown in Fig. 14a. All the Group 1 methods, as well as Group 2 (shown in Fig. 14b), seemed free of oscillations, showing a reasonable capturing of the rarefaction wave in water (which is very steep compared with the one in air) ($x \approx 2$ m), smooth transition at the phase interface ($x \approx 5$ m), and robust capturing of the shock in air (which looks very weak) ($x \approx 6$ m). In Fig. 15a the foot of the strong rarefaction in a close-up view is shown for comparison of different flux functions. As in the previous problem, AUSM$^+$-up (1, 1) is the smoothest, followed by AUSMPW+ and also by AUSM$^+$-up (0.5, 0.5). The other methods show slight undershoots. It is seen from Fig. 15b that the Godunov solver helped to increase the smoothness of these profiles, and in the G-SLAU2 result, the undershoot in SLAU2
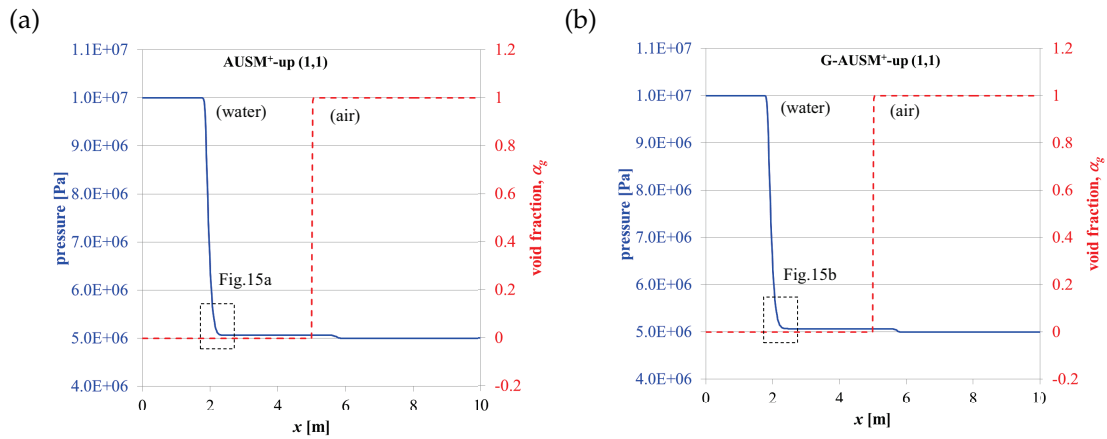
Figure 14: Water-to-air shock tube problem (with low pressure ratio, $PR=2$) solutions at $t=2$ ms, (a) AUSM$^+$-up (1, 1) (representing Group 1); (b) G-AUSM$^+$-up (1, 1) (representing Group 2).
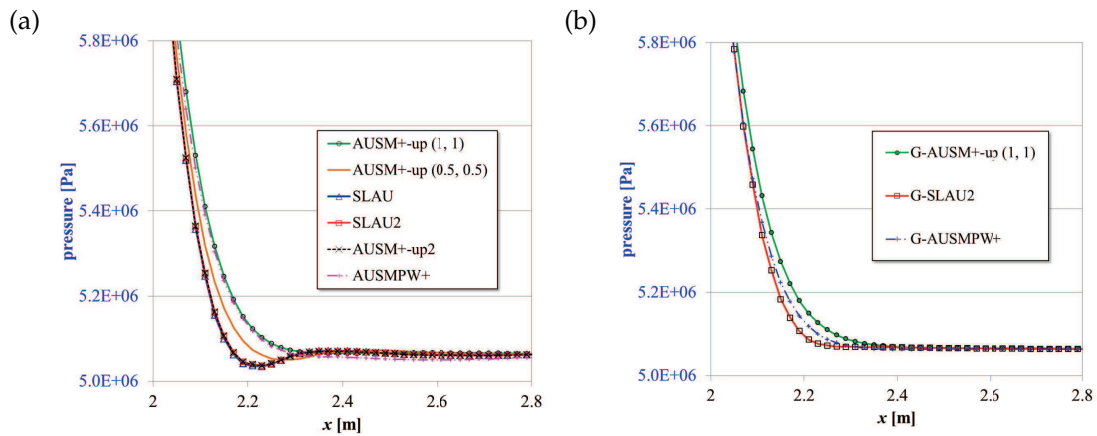

Figure 15: Magnified view of pressure profiles around foot of expansion wave in water at $t=2$ ms of the water-to-air shock tube problem (with low pressure ratio, $PR=2$), (a) Group 1; (b) Group 2.

has been corrected.

As the final grid study case, this problem was solved with:

- 5,000 cells: $\Delta x = 0.002$ m, $\Delta t = 2.0 \times 10^{-7}$ s (CFL ≈ 0.2), computed up to 2.0×10^{-3} s (10,000 steps) [*fine grid*].

The grid convergence is confirmed from the results shown in Fig. 16.

3.3.3 Water-to-Air shock tube with high pressure ratio ($PR=1,000$)

Now the same grid system is used but with higher pressure ratio, say, $PR=1,000$, as the following setup:

- $(p,\alpha_g,u_k,T_k)_L = (10^8 \text{ Pa}, \varepsilon, 0 \text{ m/s}, 308.15 \text{ K})$ for $x \leq 5$ m;

(a)

(b)

(c)

(d)
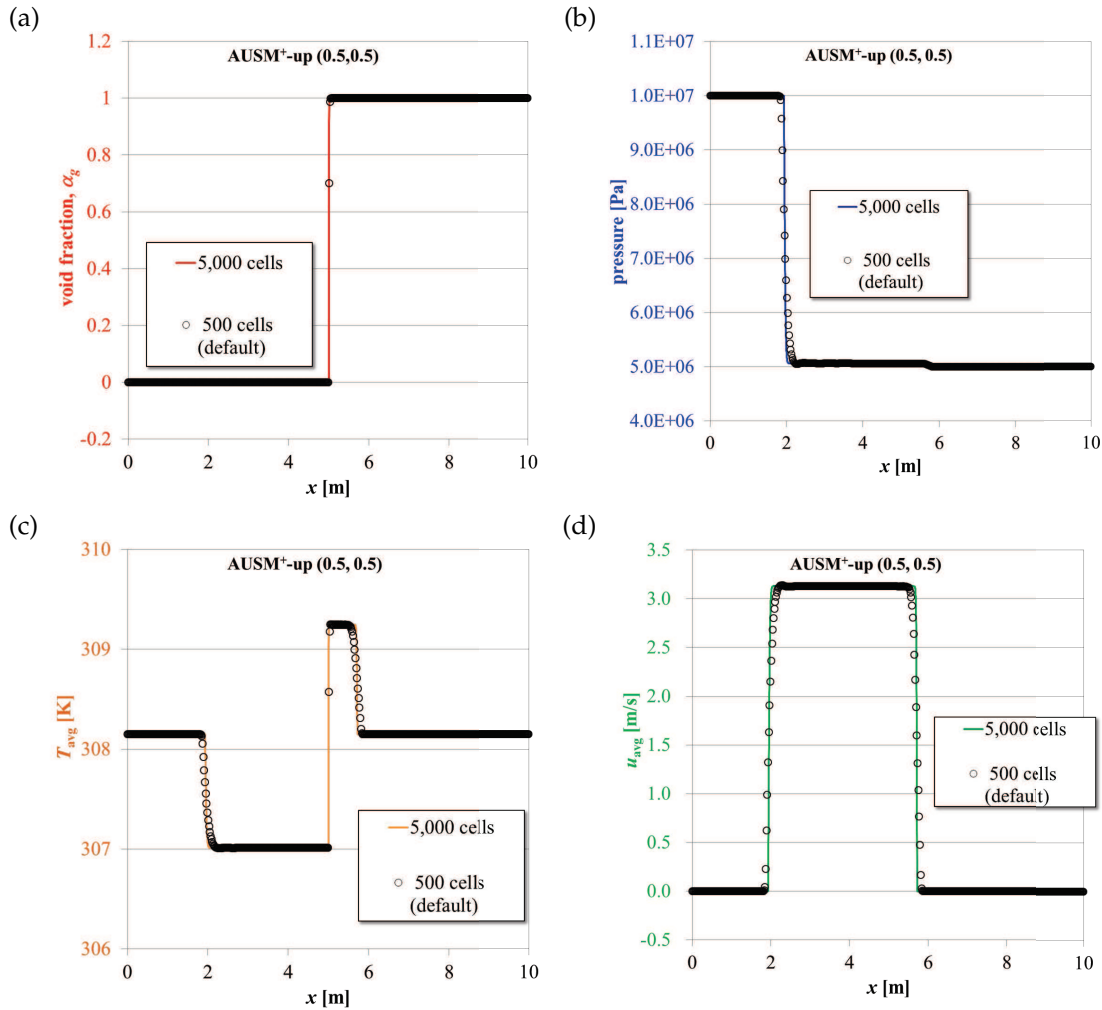
Figure 16: Solutions showing grid convergence at $t=2$ ms of the water-to-air shock tube problem of AUSM$^+$-up (0.5, 0.5), (a) Void fraction; (b) Pressure; (c) Average temperature; (d) Average velocity.

- $(p, \alpha_g, u_k, T_k)_R = (10^5 \text{ Pa}, 1-\varepsilon, 0 \text{ m/s}, 308.15 \text{ K})$ for $x > 5$ m,

where $k=g, l$, and $\varepsilon = 1.0 \times 10^{-5}$ ($\varepsilon_{\min} = 1.0 \times 10^{-7}$, $\varepsilon_{\max} = 1.0 \times 10^{-3}$).

With this high PR, all the AUSM-family schemes by itself (Group 1) failed because the severe pressure drop in the (left) water phase produced a negative pressure at the beginning of computation, as already implied in [17]. Group 2 (combination of Godunov and AUSM-family) except for G-SLAU2, on the other hand, can smooth out such a pressure decrease (Figs. 17 and 18), obviously with the help of Godunov solver as mentioned in the previous test. Thus, for such a high PR, it has been demonstrated that the Godunov solver must be used along with an AUSM-family scheme.

(a)   (b)
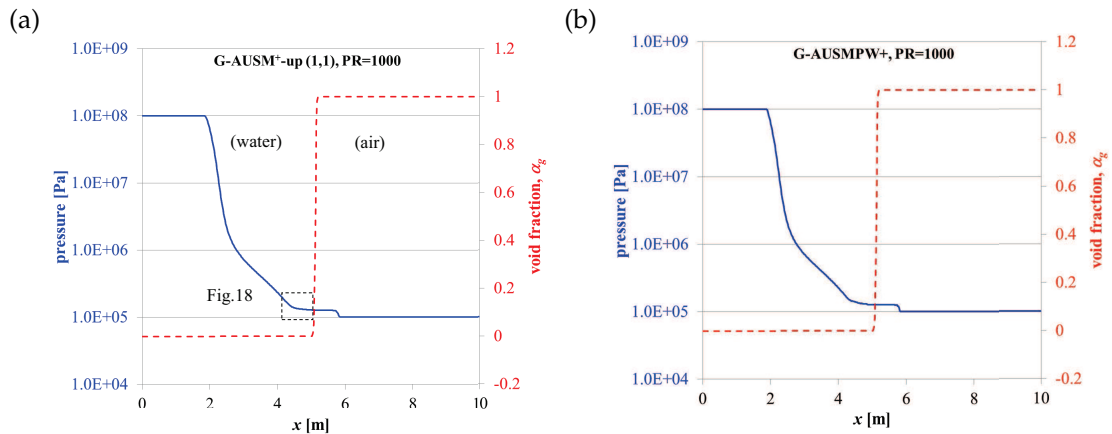
Figure 17: Water-to-air shock tube problem (with high pressure ratio, $PR = 1,000$) solutions, at $t = 2$ ms, (a) G-AUSM$^+$-up (1, 1); (b) G-AUSMPW+.
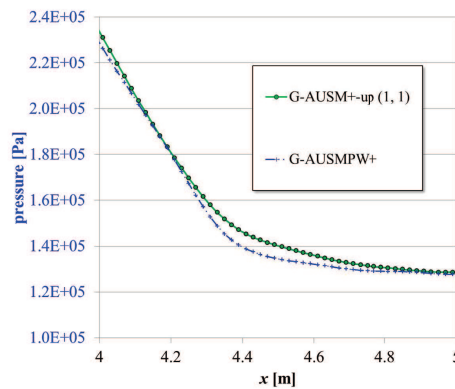

Figure 18: Magnified view of pressure profiles around foot of expansion wave in water, at $t = 2$ ms of the water-to-air shock tube problem (with high pressure ratio, $PR = 1,000$).

In addition, we conducted similar 1D problems but with more severe conditions, such as the Cases 3 and 4 in Liu et al. [56], and Case 4 in Liu et al. [57]. The results are largely similar to the ones in the current and precedent subsections: Group 1 results are acceptable only in the Case 3 in [56], whereas Group 2 results are satisfactory or near satisfactory with slight oscillations, typically resembling the ones in the original papers by Liu et al. [56,57]. Furthermore, such oscillations can be partly suppressed by employing THINC sharpening technique [32], which is ongoing in [58].

3.4   1D Cavitation Problem

This test was proposed by Saurel and Abgrall in [38], in which receding liquid flow containing 1% gas in a tube dynamically creates a cavitation zone at the center. 200 cells are

uniformly distributed over the [0m, 10m] domain (i.e., the grid spacing is $\Delta x = 0.05$ m) and the initial conditions are given as:

- $(p, \alpha_g, u_k, T_k)_L = (10^5$ Pa, ε, -100 m/s, 300 K) for $x \leq 5$ m;
- $(p, \alpha_g, u_k, T_k)_R = (10^5$ Pa, ε, 100 m/s, 300 K) for $x > 5$ m,

where $k = g, l$, and $\varepsilon = 1.0 \times 10^{-2}$ ($\varepsilon_{min} = 1.0 \times 10^{-3}$, $\varepsilon_{max} = 1.0 \times 10^{-1}$). The computations are conducted with $\Delta t = 5.0 \times 10^{-6}$ s (CFL ≈ 0.16), up to 25 ms (5,000 steps).

Figs. 19 and 20 show only the selected results (differences due to flux functions were minor). Consistent with the finding by Saurel and Abgrall, who employed an elaborate relaxation method, all the fluxes used here are "*capable of dynamically creating interfaces, even starting from a situation in which interfaces are not present*". [38]. This feature motivates us to compute a more realistic cavitation problem in the near future. It is noted that the feet of the void fraction profiles are not very smooth as those in the others' work (e.g., [38]). However, as proved by Theofanous and Chang [59], the method in [38] has huge dissipation due to their relaxation term. Obtaining smooth solutions without relying upon too much dissipation is left as the future work.

3.5 Shock/Water-Column interaction

A shock in air impacting a water column (i.e., 2D droplet) is simulated. 400×200 isotropic cells are used for a domain of $[-5$ mm, 5 mm$] \times [0$ mm, 5 mm$]$ to cover the 6.4-mm-diameter water column with its center at the origin (i.e., the diameter being 256 times grid spacing $\Delta x_{min} = \Delta y_{min} = 0.025$ mm in this region); then the cells are stretched toward outer boundaries so that a domain of $[-15$ mm, 20 mm$] \times [0$ mm, 15 mm$]$ is filled with 900×300 cells in total. Note that this grid system was generated for the purpose of resolving only early stages of evolution of large-scale structures.

The initial conditions are same as in [16]:

- $(p, \alpha_g, u_k, T_k)_L = (2.35438 \times 10^5$ Pa, ε, 225.86 m/s, 0 m/s, 381.85 K) for $x \leq -4$ mm;
- $(p, \alpha_g, u_k, T_k)_R = (1 \times 10^5$ Pa, ε, 0 m/s, 0 m/s, 293.15 K) for $x > -4$ mm, except for $x^2 + y^2 < (3.2mm)^2$ where $\alpha_g = 1 - \varepsilon$,

where $k = g, l$, and $\varepsilon = 1.0 \times 10^{-5}$ ($\varepsilon_{min} = 1.0 \times 10^{-5}$, $\varepsilon_{max} = 1.0 \times 10^{-4}$). Then the shock starts to move with $M_{sh} = 1.47$ at $t = 0$, and hits the water-column at $t \approx 1.5 \mu s$. The computations are carried out with $\Delta t = 1.25 \times 10^{-9}$ s (CFL ≈ 0.15) up to 6.25 s (5,000 steps).

To specify a smooth distribution of void fraction at the interface of the circular water column on a rectangular (Cartesian) grid, it is necessary to create a transition region of certain width, $\pm 2 \Delta x_{min}$ in this study, about the interface. The same formula used for the "vanishing" phase treatment again is applied here.

$$\left(\alpha_g \right)_{adjust} = G(\xi_2) \cdot \varepsilon + (1 - G(\xi_2)) \cdot (1 - \varepsilon), \tag{3.3a}$$

$$G(\xi_2) = -\xi_2^2 (2\xi_2 - 3), \tag{3.3b}$$

$$\xi_2 = \frac{\sqrt{x^2 + y^2} - (r - 2\Delta x_{min})}{4\Delta x_{min}}, \quad r - 2\Delta x_{min} \leq \sqrt{x^2 + y^2} \leq r + 2\Delta x_{min}, \quad r = 3.2mm. \tag{3.3c}$$
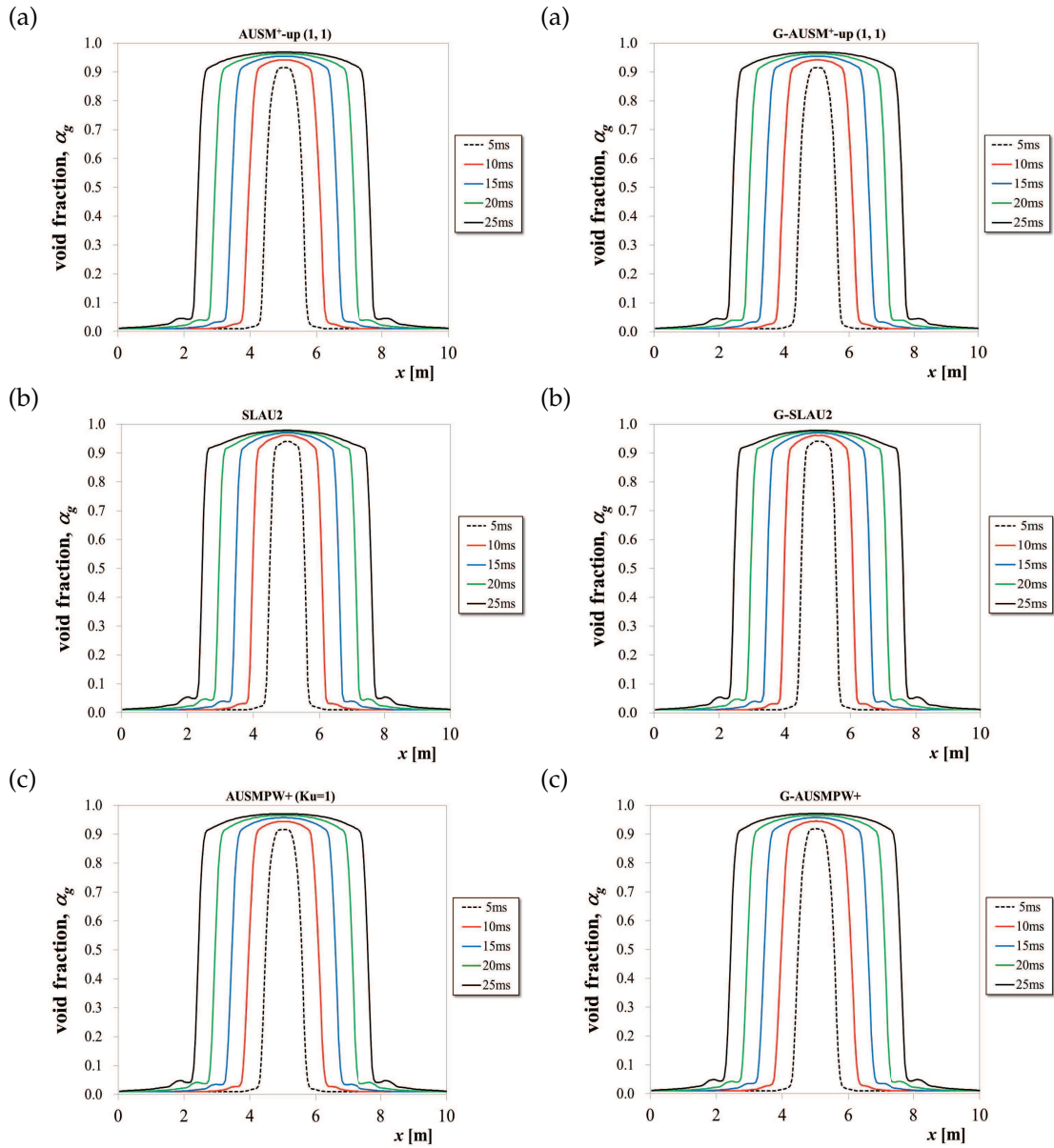
Figure 19: 1D cavitation problem α_g (void fraction) results (Group 1) at $t = 5$, 10, 15, 20, and 25 ms, (a) AUSM$^+$-up (1,1); (b) SLAU2; (c) AUSMPW+.

Figure 20: 1D cavitation problem α_g (void fraction) results (Group 2) at $t = 5$, 10, 15, 20, and 25 ms, (a) G-AUSM$^+$-up (1,1); (b) G-SLAU2; (c) G-AUSMPW+.

At the bottom boundary, the conventional slip condition is imposed; that is, only the y-component velocity is reflected, and the other variables are simply extrapolated from the interior cells. Treatments at the other boundaries are typical: the left boundary is the

(a)   (b)
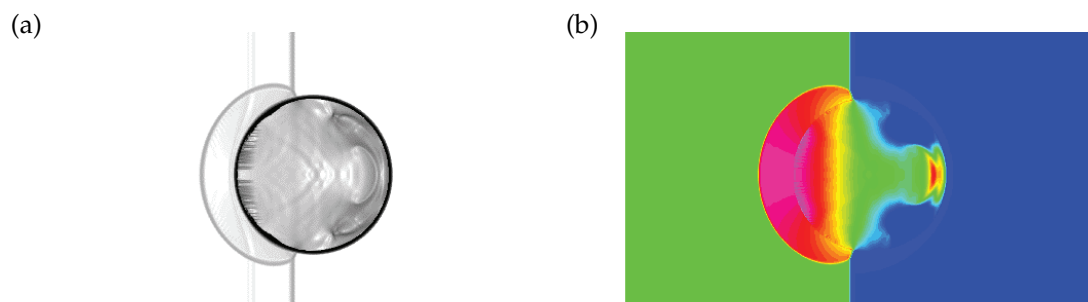
Figure 21: Time evolution of solution of shock/water-droplet interaction problem of AUSM$^+$-up (1, 1) (Group 1), (a) t=6.25μs (numerical Schlieren); (b) t=6.25μs (pressure).

(a)   (b)
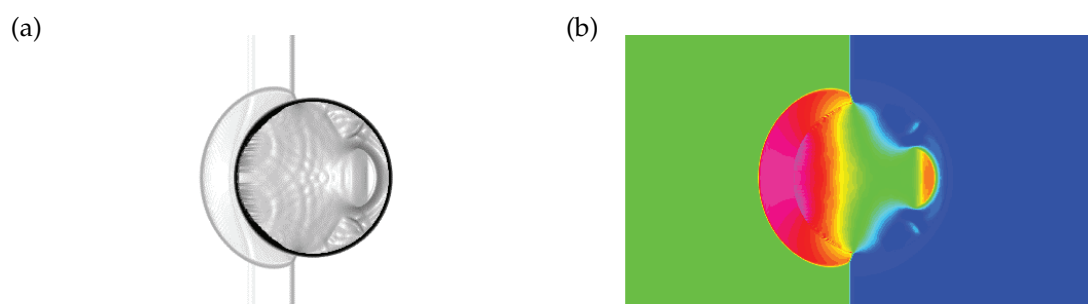
Figure 22: Time evolution of solution of shock/water-droplet interaction problem of AUSM$^+$-up (0.5, 0.5) (Group 1), (a) t=6.25μs (numerical Schlieren); (b) t=6.75μs (pressure).

inlet condition, the right is the outlet, and the top boundary is the side. Those far-field boundaries are far enough away from the water column to influence the flow of interest, and variables there are fixed in time.

The Group 1 results at t=6.25μs are shown in Figs. 21-26 (in which numerical Schlieren function $(1+\alpha_l^2)\log(|\nabla\rho|+1)$ [17] is used with the range between 4 and 20 along with pressure between 10,000 and 50,000 Pa) for AUSM$^+$-up (1, 1), AUSM$^+$-up (0.5, 0.5), SLAU2, AUSM$^+$-up2, SLAU, and AUSMPW+. AUSM$^+$-up (0, 0) was unable to compute this problem.

AUSM$^+$-up (1, 1) and AUSM$^+$-up (0.5, 0.5) both show slight noises at the front of the water column in the numerical Schlieren plots (Figs. 21a and 22a), but pressure contours (Figs. 21b and 22b) are similar to the results observed in [16]; SLAU2, AUSM$^+$-up2, and SLAU exhibit weak, high-frequency waves inside the water column (Figs.23a, 24a, 25a) that are not observed in the pressure profiles (Figs. 23b, 24b, 25b). AUSMPW+ seems free from those oscillations (Fig. 26). In spite of these, with the current grid resolution, those fluxes at least captured large-scale structures, and the results appeared to be fair.

In order for the Group 1 fluxes to proceed further in time evolution, a finer mesh is required to resolve small-scale structures, as done in [50] by halving the grid spacing in each direction (the grid spacing there was mislabeled, but it was actually $\Delta x_{\min}=\Delta y_{\min}=$

(a)   (b)
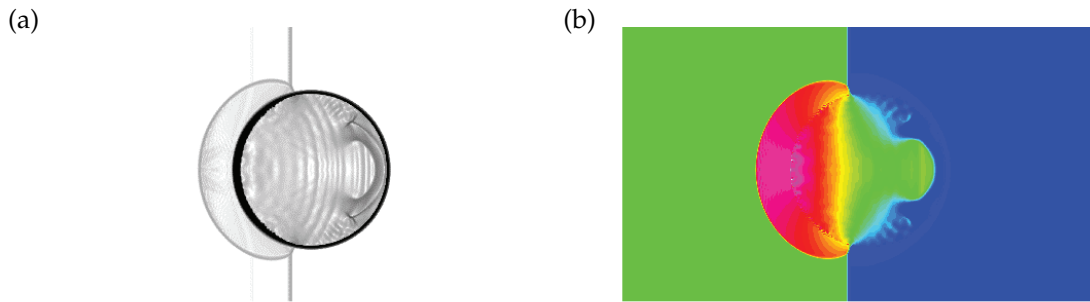
Figure 23: Time evolution of solution of shock/water-droplet interaction problem of SLAU2 (Group 1), (a) $t=6.25\mu$s (numerical Schlieren); (b) $t=6.25\mu$s s (pressure).

(a)   (b)
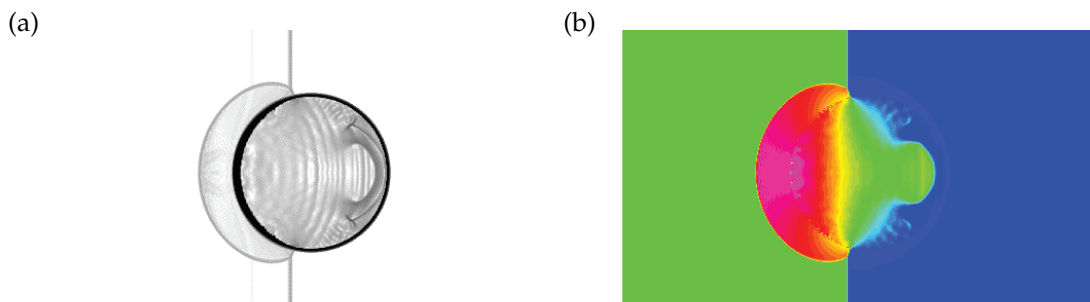
Figure 24: Time evolution of solution of shock/water-droplet interaction problem of AUSM$^+$-up2 (Group 1), (a) $t=6.25\mu$s (numerical Schlieren); (b) $t=6.25\mu$s (pressure).

(a)   (b)
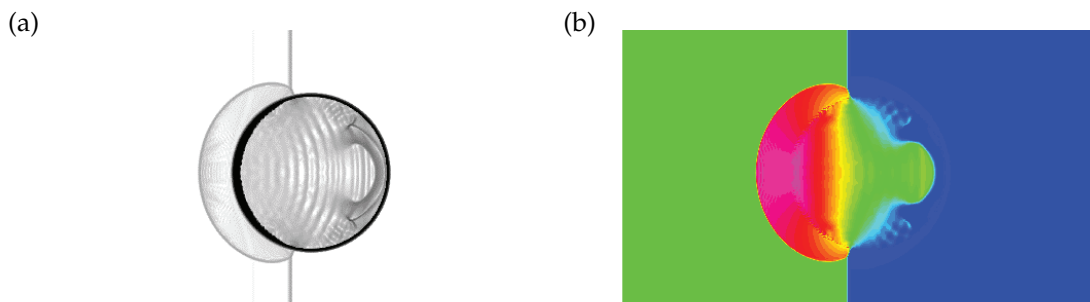
Figure 25: Time evolution of solution of shock/water-droplet interaction problem of SLAU (Group 1), (a) $t=6.25\mu$s (numerical Schlieren); (b) $t=6.25\mu$s (pressure).

0.0125 mm) and stopping at 10μs (8,000 steps). The Group 2 methods, on the contrary, were able to compute this problem longer with the initial grid. The Group 2 results up to $t=18.75\mu$s (15,000 steps) are shown in Figs. 27-29.

In G-AUSM$^+$-up (1,1), after impacting the water column, the shock transmits into the water region; in the air region, on the other hand, it diffracts as if it began to glance around a solid object. Then, the shock travels faster inside the water column than outside of it because of the greater speed of sound. At $t=6.75\mu$s, the shock inside the water

(a)   (b)
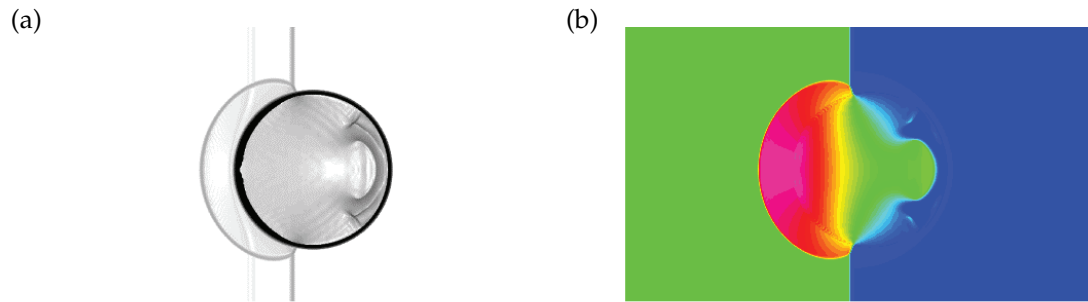
Figure 26: Time evolution of solution of shock/water-droplet interaction problem of AUSMPW+ (Group 1), (a) $t=6.25\mu s$ (numerical Schlieren); (b) $t=6.25\mu s$ (pressure).

(a)   (b)

(c)   (d)
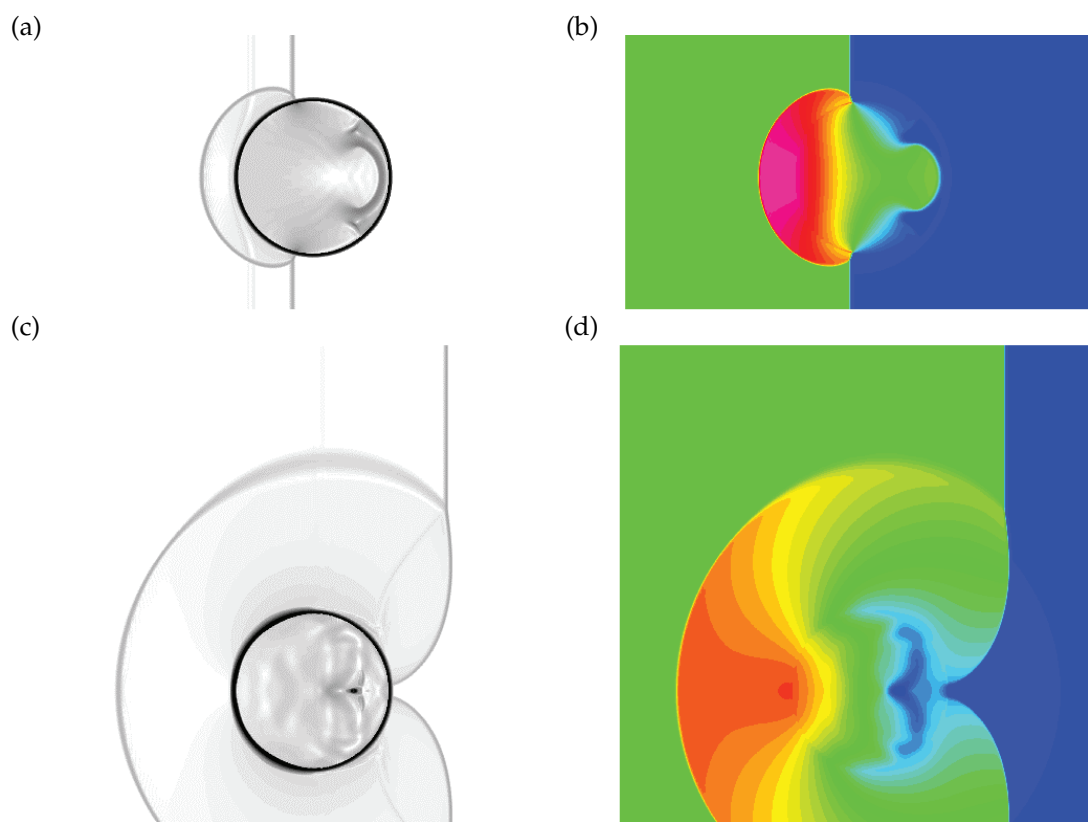
Figure 27: Time evolution of solution of shock/water-droplet interaction problem of G-AUSM$^+$-up (1,1) (Group 2), (a) $t=6.25\mu s$ (numerical Schlieren); (b) $t=6.25\mu s$ (pressure); (c) $t=18.75\mu s$ (numerical Schlieren); (d) $t=18.75\mu s$ (pressure).

column has reflected from the rear face (Figs. 27a-b). After that, the wave inside the water reflects back and forth, while the initial shock and the diffracted shock outside the water column grow almost independently (Figs. 27c-d), with little influence from

(a)

(b)

(c)

(d)
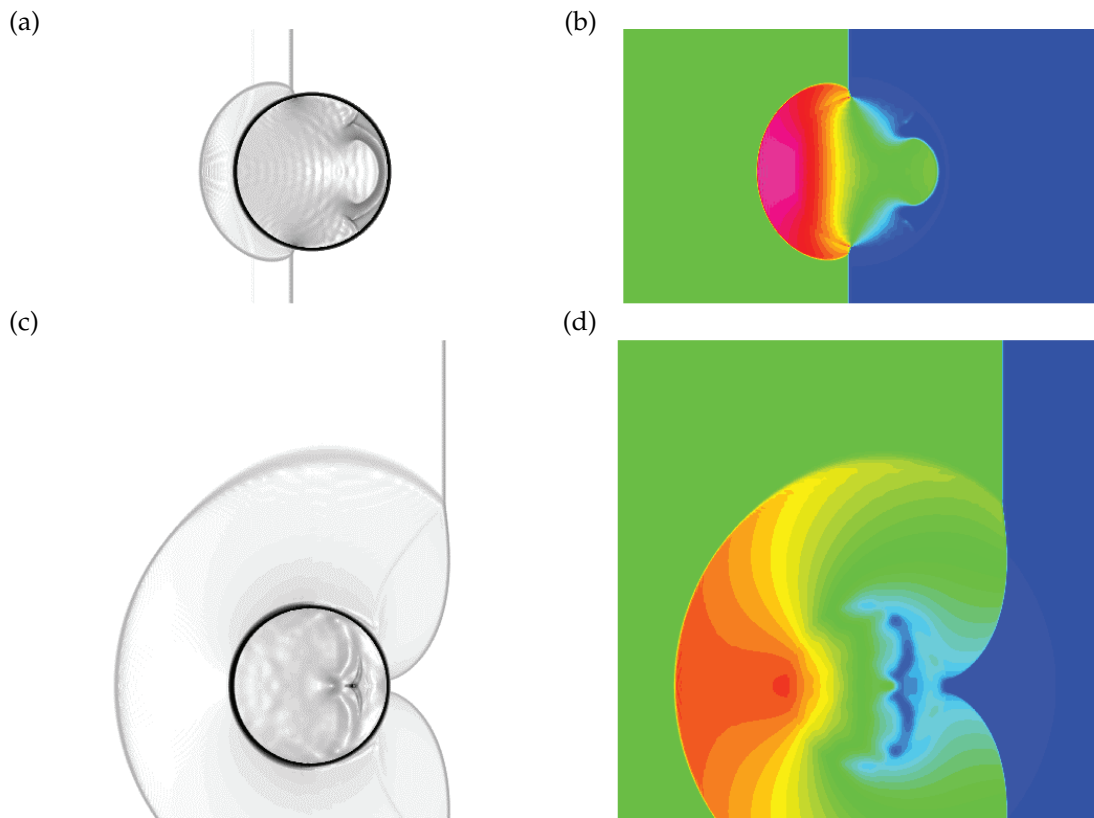
Figure 28: Time evolution of solution of shock/water-droplet interaction problem of G-SLAU2 (Group 2), (a) $t=6.25\mu$s (numerical Schlieren); (b) $t=6.25\mu$s (pressure); (c) $t=18.75\mu$s (numerical Schlieren); (d) $t=18.75\mu$s (pressure).

the flow inside. Similar evolutions of solutions are found for G-SLAU2 (Fig. 28) and G-AUSMPW+ (Fig. 29), although high-frequency waves (weaker than in Group 1 cases) can still be seen in the early stages, $t=6.25\mu$s (Figs. 28a-b and 29a-b).

In summary, all the schemes tested are used for this 2D challenging shock/water column interaction problem, at least at the early stages with limited grid points (Group 1). When the Godunov solver is included (Group 2), longer simulations are possible on the same grid with smooth solutions. The differences in solutions are minor among the selected AUSM-family schemes, but with the smoothness/diffusiveness in the following order: AUSMPW+, AUSM^{+}-up (1,1), AUSM^{+}-up (0.5,0.5), SLAU2 (or AUSM^{+}-up2), and SLAU in Group 1; G-AUSM^{+}-up (1,1), and G-SLAU2 or G-AUSMPW+ in Group 2.

3.6 Shock/Air-Bubble interaction

This test is opposite to the previous test, with a water shock impacting a column of an air bubble, but with a much higher pressure ratio ($PR \approx 1.6 \times 10^4$). The grid system is the

(a)

(b)

(c)

(d)
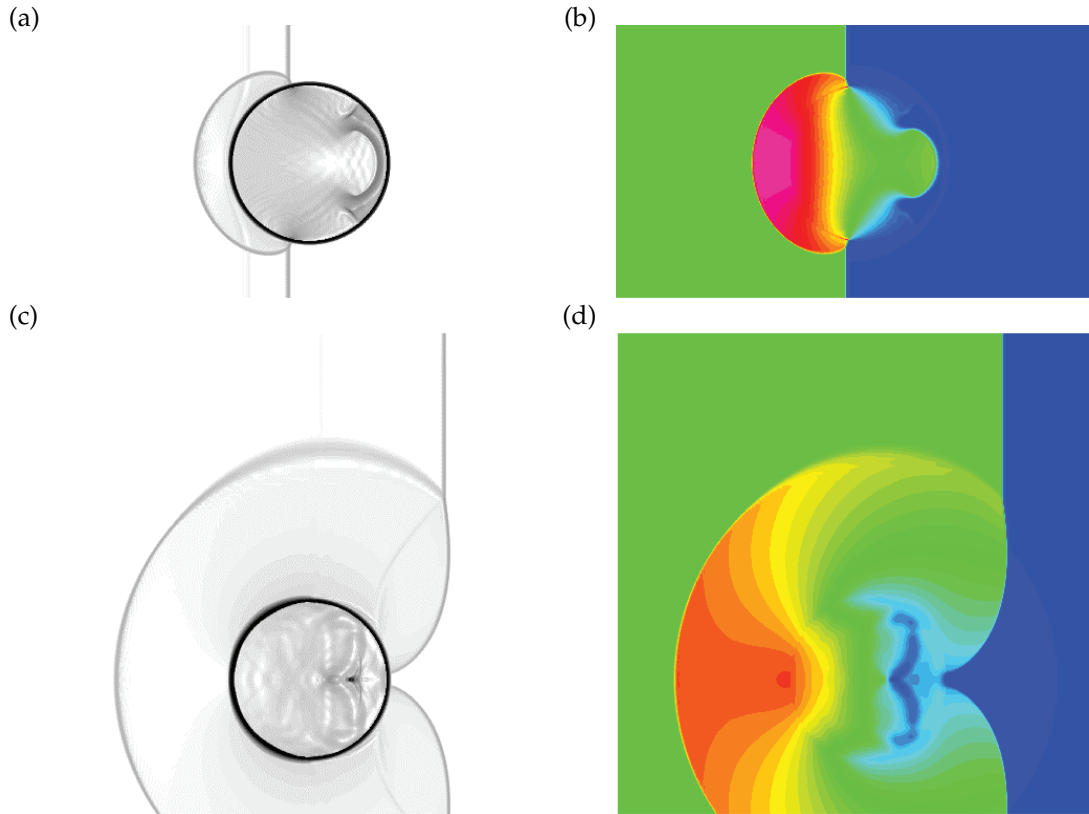
Figure 29: Time evolution of solution of shock/water-droplet interaction problem of G-AUSMPW+ (Group 2), (a) $t=6.25\mu$s (numerical Schlieren); (b) $t=6.25\mu$s (pressure); (c) $t=18.75\mu$s (numerical Schlieren); (d) $t=18.75\mu$s (pressure).

same as that in the shock/water column interaction problem. The initial conditions are the same as in [17]:

- $(p,\alpha_g,u_k,v_k,T_k)_L=(1.6\times10^9$ Pa, $1-\varepsilon$, 661.81 m/s, 0 m/s, 595.13 K) for $x\leq-4$ mm;

- $(p,\alpha_g,u_k,v_k,T_k)_R=(1.01325\times10^5$ Pa, $1-\varepsilon$, 0 m/s, 0 m/s, 292.98 K) for $x>-4$ mm, except for $x^2+y^2<3.2$ mm^2 where $\alpha_g=\varepsilon=1.0\times10^{-3}$ ($\varepsilon_{min}=1.0\times10^{-3}$, $\varepsilon_{max}=1.0\times10^{-1}$).

The shock moves at $M_{sh}=1.51$ at $t=0$ and hits the air bubble at $t\approx0.3$ μs. The computations are carried out with $\Delta t=3.125\times10^{-10}$ s (CFL ≈0.05) up to 5.0μs (16,000 steps).The results of G-AUSM$^+$-up (1,1) (only in this case, a threshold for effective length is 5ε, and the speed of sound is defined individually for each phase; otherwise, the problem was not computed) and G-SLAU2 are shown in Figs. 30 and 31 (in which numerical Schlieren function $\log(|\nabla\rho|+1)$ [17] is used with the range between 8 and 14 and with pressure between 10^8 and 2×10^9 Pa), respectively; Group 1 and G-AUSMPW+ cases blew up immediately after the shock hit the bubble. The presented two sets of results agree with
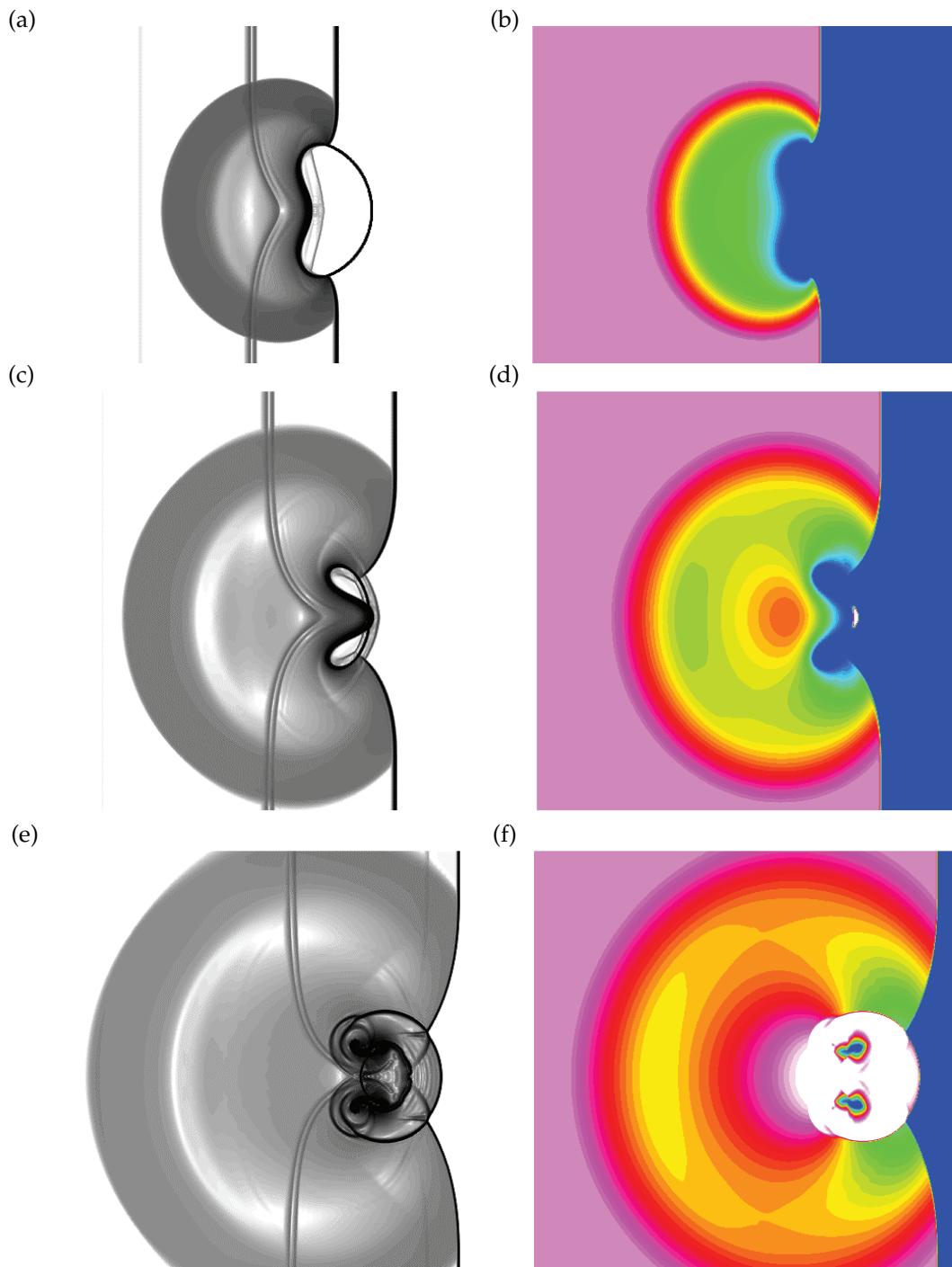
Figure 30: Time evolution of solution of shock/air-bubble interaction problem of G-AUSM$^+$-up (1,1) (Group 2), (a) $t=2.5\mu$s (numerical Schlieren); (b) $t=2.5\mu$s (pressure); (c) $t=3.75\mu$s (numerical Schlieren); (d) $t=3.75\mu$s (pressure); (e) $t=5.0\mu$s (numerical Schlieren); (f) $t=5.0\mu$s (numerical Schlieren).

(a)

(b)

(c)

(d)

(e)

(f)
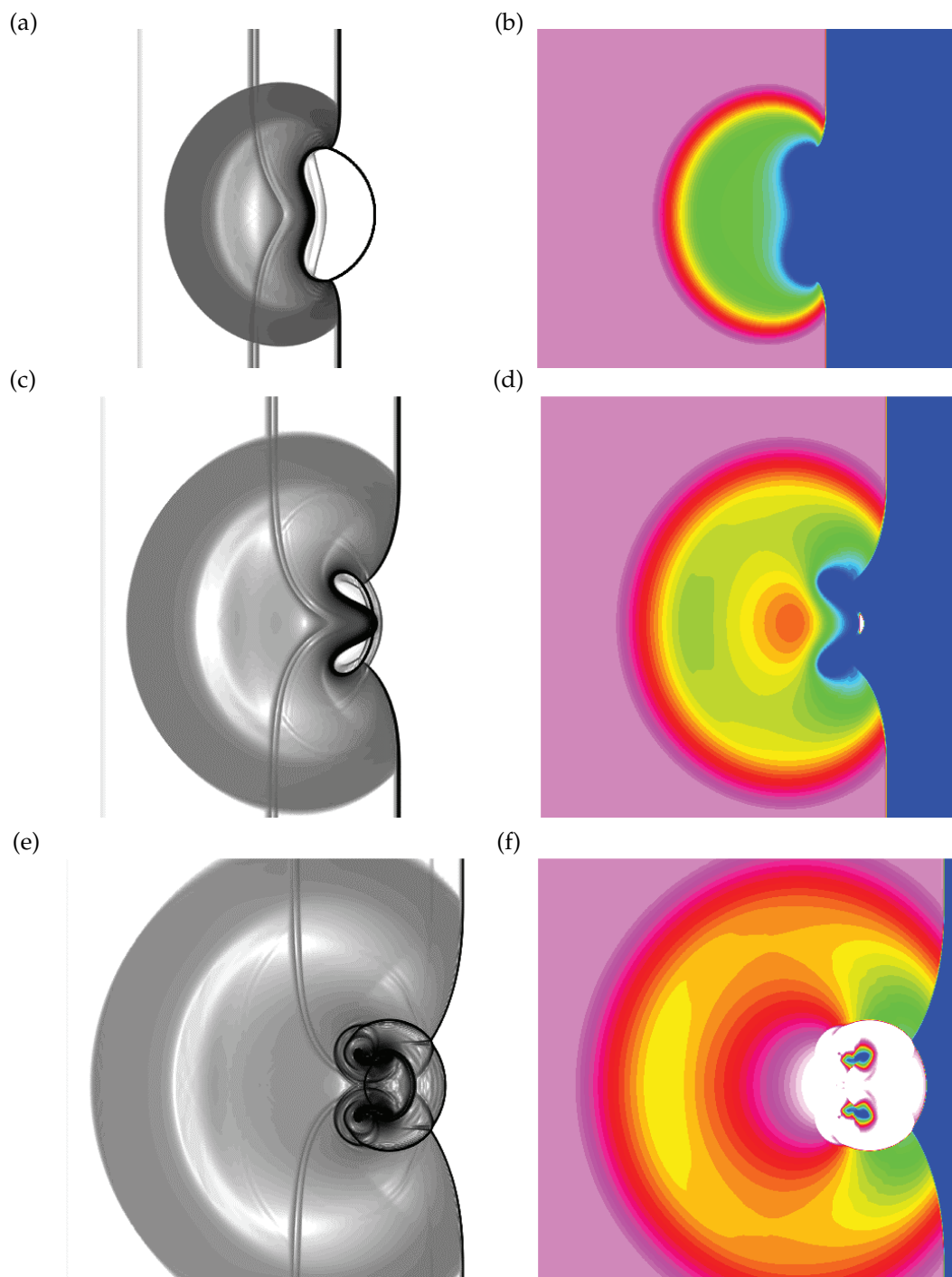
Figure 31: Time evolution of solution of shock/air-bubble interaction problem of G-SLAU2 (Group 2), (a) $t = 2.5\mu$s (numerical Schlieren); (b) $t = 2.5\mu$s (pressure); (c) $t = 3.75\mu$s (numerical Schlieren); (d) $t = 3.75\mu$s (pressure); (e) $t = 5.0\mu$s (numerical Schlieren); (f) $t = 5.0\mu$s (numerical Schlieren).

each other, suggesting that the choice of an AUSM-family scheme in Group 2 affects the robustness of the computation, but does not have a strong impact on the solutions. As time progresses in both results, the left rim of the air bubble is pushed forward (to the right), and it is deformed and compressed into a smaller volume (Figs. 30a-b and 31a-b). After the left rim of the bubble reaches the right rim, the pressure there begins to exceed the water ambient pressure (up to 2.9×10^9 Pa at 3.75μs, Figs. 30c-d and 31c-d), thereby pushing the surrounding fluids away. Subsequently, the bubble is broken into two separate bubbles, which are still resolved well by the current grid (5.0μs, Figs. 30e-f and 31e-f). Further details are explained by Chang and Liou in [17].

All in all, it has been demonstrated from all the above problems that AUSM-family fluxes have been successfully extended within the same two-fluid framework [16, 17] and provide reliable results in most cases, including shock/water-column or shock/air-bubble interaction. The results of all the tests with all the flux functions are summarized in Tables 1 and 2 for Groups 1 and 2, respectively, with the order of smoothness of solutions from top to bottom, in general.

4 Conclusions

In this work, recently developed AUSM-family numerical flux functions (SLAU, SLAU2, AUSM$^+$-up2, and AUSMPW+) have been successfully extended to compressible multiphase flow computations, based on the stratified flow model concept, following Liou et al. [16] (in which AUSM$^+$-up was used standalone) and Chang and Liou [17] (in which the exact Riemann solver was combined). Then, we performed an extensive survey using those flux functions. The key findings are as follows:

1. AUSM$^+$-up with sufficient dissipations ($K_p = 1.0$, $K_u = 1.0$) and ($K_p = 0.5$, $K_u = 0.5$), AUSMPW+, SLAU2 or AUSM$^+$-up2 ($K_p = 1$), and SLAU can be used (in this order of smoothness/diffusivity of solutions), even for a challenging 2D shock/water-droplet interaction.

2. SLAU showed oscillatory behaviors [though not as catastrophic as those of AUSM$^+$ (equivalent to setting $K_p = K_u = 0$ in AUSM$^+$-up)] because of insufficient dissipation arising from the ideal-gas-based dissipation term.

3. When combined with the exact Riemann solver as suggested in [17], the robustness of each AUSM-family scheme has been greatly enhanced at a phase interface. Specifically, capabilities for solving shock tube and shock/air-bubble interaction problems involving a high pressure ratio (1,000 or more) have been confirmed. It has also been found that the choice of the partner AUSM-family scheme affects the robustness of the computation, but does not have significant impact on the solutions. In combination with the exact Riemann solver, AUSM$^+$-up (1,1) yielded smoother results than SLAU2 and AUSMPW+ did, and appears to be the most robust.

Table 1: List of solutions of test problems (Group 1) (S: Successful, A: Acceptable, F: Failure) (div. = divergence).

Flux functions	Moving phase disconti- nuity	Faucet problem	Air-to- water shock tube	Water-to- air shock tube	Water-to- air shock tube with high PR	1D cavitation	Shock/ water- column inter- action	Shock/ air- bubble inter- action
AUSM$^+$-up (1, 1)	S	S	S	S	F (div.)	S	A	F (div.)
AUSM$^+$-up(0.5, 0.5)	S	S	S	S	F (div.)	S	A	F (div.)
AUSMPW+	S	S	A (slight osci- llation)	S	F (div.)	S	A	F (div.)
SLAU2 or AUSM$^+$-up2	S	S	S	A (slight under- -shoot)	F (div.)	S	A (weak osci-) llation)	F (div.)
SLAU	S	S	A (slight osci- llation)	A (slight under- shoot)	F (div.)	S	A (weak osci- llation)	F (div.)

Table 2: List of solutions of test problems (Group 2) (S: Successful, A: Acceptable, F: Failure) (div. = divergence).

Flux functions	Moving phase disconti- nuity	Faucet problem	Air-to- water shock tube	Water-to- air shock tube	Water-to- air shock tube with high PR	1D cavitation	Shock/ water- column inter- action	Shock/ air- bubble inter- action
G-AUSM$^+$-up(1, 1)	S	S	S	S	S	S	S	S
G-SLAU2	S	S	S	S	F (div.)	S	S	S
G-AUSMPW+	S	S	A (slight osci- llation)	S	S	S	S	F (div.)

4. It has been demonstrated that a cavitation zone is automatically created by the present two-fluid approach. This fact has encouraged us proceed to more realistic cavitation applications, and the research in this direction is ongoing.

The results and discoveries herein will serve as a useful guideline for users when choosing fluxes and as a reference for further developments of numerical modeling of multiphase flows.

Acknowledgments

References

[1] Peery, K.M., and Imlay, S.T., Blunt-Body Flow Simulations, AIAA Paper 88-2904, 1988.

[2] Pandolfi, M., and D'Ambrosio, D., Numerical Instabilities in Upwind Methods: Analysis and Cures for the Carbuncle Phenomenon, *J. Comput. Phys.*, Vol. 166, No. 2, 2001, pp. 271-301. doi:10.1006/jcph.2000.6652.

[3] Liou, M.S., Mass Flux Schemes and Connection to Shock Instability, *J. Comput. Phys.*, Vol. 160, 2000, pp. 623-648.

[4] Kitamura, K., Roe, P., and Ismail, F., Evaluation of Euler Fluxes for Hypersonic Flow Computations, *AIAA J.*, Vol. 47, 2009, pp. 44-53.

[5] Gnoffo, P.A., Multidimensional, Inviscid Flux Reconstruction for Simulation of Hypersonic Heating on Tetrahedral Grids, AIAA Paper 2009-599, 2009.

[6] Candler, G.V., Mavriplis, D.J., and Treviño, L., Current Status and Future Prospects for the Numerical Simulation of Hypersonic Flows, AIAA Paper 2009-153, 2009.

[7] Kitamura, K., Shima, E., Nakamura, Y., and Roe, P., Evaluation of Euler Fluxes for Hypersonic Heating Computations, *AIAA J.*, Vol. 48, 2010, pp. 763-776. doi:10.2514/1.41605.

[8] Kitamura, K., Shima, E., and Roe, P., Carbuncle Phenomena and Other Shock Anomalies in Three Dimensions, *AIAA J.*, Vol. 50, 2012, pp. 2655-2669. doi:10.2514/1.J051227.

[9] Turkel, E., Preconditioning Technique in Computational Fluid Dynamics, *Annual Review of Fluid Mechanics*, Vol. 31, 1999, pp. 385-416.

[10] Weiss, J.M., and Smith, W.A., Preconditioning Applied to Variable and Constant Density Flows, *AIAA J.*, Vol. 33, No.11, 1995, pp. 2050-2057.

[11] Liou, M.-S., A Sequel to AUSM, Part II: AUSM$^+$-up for All Speeds, *J. Comput. Phys.*, Vol. 214, 2006, pp. 137-170.

[12] Shima, E., and Kitamura, K., Parameter-Free Simple Low-Dissipation AUSM-Family Scheme for All Speeds, *AIAA J.*, Vol. 49, No. 8, 2011, pp. 1693-1709. doi:10.2514/1.55308.

[13] Hosangadi, A., Sachdev, J., and Sankaran, V., Improved Flux Formulations for Unsteady Low Mach Number Flows, ICCFD7-2202, Seventh International Conference on Computational Fluid Dynamics (ICCFD7), Big Island, Hawaii, July 9-13, 2012.

[14] Kitamura, K., Shima, E., Fujimoto, K., and Wang, Z.J., Performance of Low-Dissipation Euler Fluxes and Preconditioned LU-SGS at Low Speeds, *Commun. Comput. Phys.*, Vol. 10, No. 1, 2011, pp. 90-119.

[15] Kitamura, K., and Shima, E., Improvements of Simple Low-dissipation AUSM against Shock Instabilities in consideration of Interfacial Speed of Sound, V European Conference on Computational Fluid Dynamics, ECCOMAS CFD 2010, 2010.

[16] Liou, M.-S., Chang, C.-H., Nguyen, L., and Theofanous, T. G., How to Solve Compressible Multifluid Equations: A Simple, Robust, and Accurate Method, *AIAA J.*, Vol. 46, 2008, pp. 2345-2356.

[17] Chang, C.-H., and Liou, M.-S, A Robust and Accurate Approach to Computing Compressible Multiphase Flow: Stratified Flow Model and AUSM$^+$-up Scheme, *J. Comput. Phys.*, Vol. 225, 2007, pp. 840-873.

[18] Chang, C.-H., and Liou, M.-S., A New Approach to the Simulation of Compressible Multiphase Flows with AUSM$^+$ Scheme, AIAA Paper 2003-4107, 2003.

[19] Niu, Y.-Y., Lin, Y.-C., and Chang, C.-H., A Further Work on Multi-Phase Two-Fluid Approach for Compressible Multi-Phase Flows, *Int. J. Numer. Meth. Fluids*, Vol. 58, 2008, pp. 879-896.

[20] Paillère, H., Corre, C., and Cascales, J.R.G., On the Extension of the AUSM$^+$ Scheme to Compressible Two-Fluid Models, *Comput. Fluids*, Vol. 32, 2003, pp. 891-916.

[21] Stewart, H.B., and Wendroff, B., Two-Phase Flow: Models and Methods, *J. Comput. Phys.*, Vol. 56, 1984, pp. 363-409.

[22] Liou, M.-S., A Sequel to AUSM: AUSM$^+$, *J. Comput. Phys.*, Vol. 129, 1996, pp. 364-382.

[23] Kitamura, K., and Shima, E., Towards shock-stable and accurate hypersonic heating computations: A new pressure flux for AUSM-family schemes, *J. Comput. Phys.*, Vol. 245, 2013, pp. 62-83. doi: 10.1016/j.jcp.2013.02.046.

[24] Kim, S.S., Kim, C., Rho, O.H., Hong, S.K., Methods for the Accurate Computations of Hypersonic Flows I. AUSMPW+ Scheme, *J. Comput. Phys.*, Vol. 174, 2001, pp. 38-80.

[25] Godunov, S.K., A Finite Difference Method for the Numerical Computation of Discontinuous Solutions of the Equations of Fluid Dynamics, *Matematicheskii Sbornik/Izdavaemyi Moskovskim Matematicheskim Obshchestvom*, Vol. 47, No. 3, 1959, pp. 271-306.

[26] Osher, S., and Sethian, J.A., Fronts Propagating with Curvature Dependent Speed: Algorithms Based on Hamilton-Jacobi Formulations, *J. Comput. Phys.*, Vol. 79, 1988, pp. 12-49.

[27] Sussman, M., Smereka, P., and Osher, S., A Level Set Approach for Computing Solutions to Incompressible Two-Phase Flow, *J. Comput. Phys.*, Vol. 114, 1994, pp. 146-159.

[28] Kim, H., and Liou, M.-S., Accurate Adaptive Level Set Method and Sharpening Technique for Three Dimensional Deforming Interfaces, *Comput. Fluids*, Vol. 44, 2011, pp. 111-129.

[29] Tryggvason, G., Bunner, B., Esmaeeli, A., Juric, D., Al-Rawahi, N., Tauber, W., Han, J., Nas, S., and Jan, Y.-J., A Front-Tracking Method for the Computations of Multiphase Flow, *J. Comput. Phys.*, Vol. 169, 2001, pp. 708-759.

[30] Terashima, H., and Tryggvason, G., A Front-Tracking/Ghost-Fluid Method for Fluid Interfaces in Compressible Flows, *J. Comput. Phys.*, Vol. 228, 2009, pp. 4012-4037.

[31] Hirt, C.W., and Nichols, B.D., Volume of Fluid (VOF) Method for the Dynamics of Free Boundaries, *J. Comput. Phys.*, Vol. 39, No. 1, 1981, pp. 201-225. doi:10.1016/0021-9991(81)90145-5.

[32] Ii, S., Sugiyama, K., Takeuchi, S., Takagi, S., Matsumoto, Y., and Xiao, F., An Interface Capturing Method with a Continuous Function: The THINC Method with Multi-Dimensional Reconstruction, *J. Comput. Phys.*, Vol. 231, 2012, pp. 2328-2358.

[33] Goncalves, E., and Patella, R. F., Numerical Simulation of Cavitating Flows with Homogeneous Models, Comput. Fluids, Vol. 38, 2009, pp. 1682-1696.

[34] Edwards, J. R., Franklin, R. K., and Liou, M.-S., Low-Diffusion Flux-Splitting Methods for Real Fluid Flows with Phase Transitions, *AIAA J.*, Vol. 38, 2000, pp. 1624-1633.

[35] Ihm, S.-W., and Kim, C., Computations of Homogeneous-Equilibrium Two-Phase Flows with Accurate and Efficient Shock-Stable Schemes, *AIAA J.*, Vol. 46, 2008, pp. 3012-3037.

[36] Saurel, R., and Lemetayer, O., A Multiphase Model for Compressible Flows with Interfaces, Shocks, Detonation Waves and Cavitation, *J. Fluid Mech.*, Vol. 431, 2001, pp. 239-271.

[37] Toumi, I., An Upwind Numerical Method for Two-Fluid Two-Phase Flow Methods, *Nuclear Sci. Eng.*, Vol. 123, 1996, pp. 147-168.

[38] Saurel, R., and Abgrall, R., A Multiphase Godunov Method for Compressible Multifluid and Multiphase Flows, *J. Comput. Phys.*, Vol. 150, 1999, pp. 425-467.

[39] Chang, C.-H., Sushchikh, S., Nguyen, L., Liou, M.-S., and Theofanous, T., Hyperbolicity, Discontinuities, and Numerics of the Two-Fluid Model, 5th Joint ASME/JSME Fluids Engineering Summer Conference, American Society of Mechanical Engineers, Fluid Engineering Div., Paper FEDSM2007-37338, 2007.

[40] Shukla, R.K., Pantano, C., and Freund, J.B., An Interface Capturing Method for the Simulation of Multi-Phase Compressible Flows, *J. Comput. Phys.*, Vol. 229, 2010, pp. 7411-7439.

[41] So, K.K., Hu, X.Y., and Adams, N.A., Anti-Diffusion Interface Sharpening Technique for Two-Phase Compressible Flow Simulations, *J. Comput. Phys.*, Vol. 231, 2012, pp. 4304-4323.

[42] Kiris, C.C., Kwak, D., Chan, W., and Housman, J.A., High-Fidelity Simulations of Unsteady Flow through Turbopumps and Flowliners, *Comput. Fluids*, Vol. 37, 2008, pp. 536-546.

[43] Van Leer, B., Towards the Ultimate Conservative Difference Scheme. V. A Second-Order Sequel to Godunov's Method, *J. Comput. Phys.*, Vol. 32, 1979, pp. 101-136.

[44] Van Albada, G.D., Van Leer, B., and Roberts, Jr., W.W., A Comparative Study of Computational Methods in Cosmic Gas Dynamics, *Astron. Astrophys.*, Vol. 108, 1982, pp. 76-84.

[45] Gottlieb, S., and Shu, C.-W., Total Variation Diminishing Runge-Kutta Schemes, *Math. Comput.*, Vol. 67, 1998, pp. 73-85.

[46] Stuhmiller, J., The Influence of Interfacial Pressure Forces on the Character of Two-Phase Flow Model Equations, *Int. J. Multiphase Flow*, Vol. 3, 1977, pp. 551-60.

[47] Harlow, F., and Amsden, A., Fluid Dynamics, Technical Report LA-4700, Los Alamos National Laboratory, 1971.

[48] Jolgam, S., Ballil, A., Nowakowski, A., and Nicolleau, F., On Equations of State for Simulations of Multiphase Flows, Proc. World Congress on Engineering 2012, Vol. III, WCE 2012, July 4-6, 2012, London, U.K.

[49] Private communication with Chongam Kim, Seoul National University, Republic of Korea, August 11, 2012.

[50] Kitamura, K., and Liou, M.-S., Comparative Study of AUSM-Family Schemes in Compressible Multiphase Flow Simulations, ICCFD7-3702, Seventh International Conference on Computational Fluid Dynamics (ICCFD7), Big Island, Hawaii, July 9-13, 2012.

[51] Toro, E.F., The Riemann Problem for the Euler Equations, Riemann Solvers and Numerical Methods for Fluid Dynamics: A Practical Introduction, Third Edition, Springer-Verlag, Telos, 2009, pp. 115-162. doi:10.1007/b7976-1_4.

[52] Terashima, H., Kawai, S., and Yamanishi, N., High-Resolution Numerical Method for Supercritical Flows with Large Density Variations, *AIAA J.*, Vol. 49, No. 12, 2011, pp. 2658-2672.

[53] Roe, P.L., Characteristic-based Schemes for the Euler Equations, *Ann. Rev. Fluid Mech.*, Vol. 18, pp. 337-365.

[54] Chakravathy, S.R., and Osher, S., High Resolution Applications of the Osher Upwind Scheme for the Euler Equations, Proc. AIAA 6th Computational Fluid Dynamics Conference, AIAA Paper 83-1943, pp. 363-373, 1983.

[55] Ransom, V.H., Numerical Benchmark Tests, edited by G. F. Hewitt, J. M. Delhay, and N. Zuber, Vol. 3, Multiphase Science and Technology, Hemisphere, Washington, DC, 1987, pp. 465-467.

[56] Liu, T.G., Khoo, B.C., and Yeo, K.S., Ghost fluid method for strong shock impacting on material interface, *J. Comput. Phys.*, Vol. 190, 2003, pp. 651-681.

[57] Liu, T.G., Khoo, B.C., and Wang, C.W., The ghost fluid method for compressible gas-water simulation, J. Comput. Phys., Vol. 204, 2005, pp. 193-221.

[58] Nonomura, T., Kitamura, K., and Fujii, K., A Simple Interface Sharpening Technique with a Hyperbolic Tangent Function Applied to Compressible Two-Fluid Modeling, *J. Comput. Phys.*, Vol. 258, 2014, pp. 95-117. doi: 10.1016/j.jcp.2013.10.021.

[59] Theofanous, T., and Chang, C.-H., On the Computation of Multiphase Interactions in Transonic and Supersonic Flows, AIAA 2008-1233, 2008.